AN IMPROVED METHOD OF CALCULATING THE TIP VORTEX GEOMETRY FOR HOVERING ROTORS

A THESIS

Presented to

The Faculty of the Division of Graduate Studies

By

Satish S. Samant

In Partial Fulfillment

of the Requirements for the Degree

Doctor of Philosophy

in the School of Aerospace Engineering

GEORGIA INSTITUTE OF TECHNOLOGY

November 1976

AN IMPROVED METHOD OF CALCULATING THE TIP VORTEX GEOMETRY FOR HOVERING ROTORS

Approved:

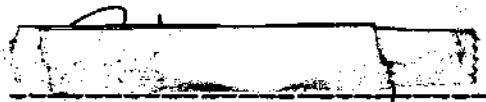

Robin B. Gray, Chairman

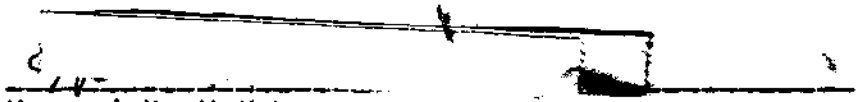

Howard M. McMahon

G. Alvin Fierce

Date approved by Chairman DECEMBER 30, 1976

ACKNOWLEDGEMENTS

The author wishes to take this opportunity to express his profound gratitude for Dr. Robin B. Gray for his valuable guidance, encouragement, and everlasting patience.

Thanks are also due to Professors H. M. McMahon, G. A. Pierce, and J. J. Harper of the School of Aerospace Engineering, and Regents' Professor P. G. Mayer of the School of Civil Engineering for their constructive criticism and valuable suggestions.

Special thanks are due to the School of Aerospace Engineering for the financial assistance provided during the course of this work.

TABLE OF CONTENTS

LIST OF SYMBOLS

a	local lift curve slope
A	contraction parameter, Eq. (III-1)
b	number of blades
c	local chord, constant in this analysis
c_l	local lift coefficient
C_T	thrust coefficient for the rotor, $C_T = \frac{T}{\rho \pi \Omega^2 R^4}$
C_Γ	tip vortex circulation strength coefficient, $C_\Gamma = \frac{\Gamma}{4\pi\Omega(RA)^2}$
$C_\Gamma(x)$	blade circulation distribution, $C_\Gamma(x) = \frac{\Gamma(x)}{4\pi\Omega(RA)^2}$
$\frac{dC_T(x)}{dx}$	nondimensional blade loading, $\frac{dC_T(x)}{dx} = \frac{dT/dr}{\rho\pi\Omega^2 R^4}$
dT/dr	sectional thrust loading
l	exponent in Eq. (II-3)
k_1	axial coordinate parameter, Eq. (III-2a)
k_2	axial coordinate parameter, Eq. (III-2b)
n	location counter in the wake
P	defined in Eqs. (III-8) and (III-11)
Q	parameter introduced in Eq. (II-3)

r	radial coordinate
R	rotor blade radius
RA	nondimensionalizing length, radius of the tip vortex in the ultimate wake
T	rotor thrust
u	nondimensional induced radial velocity
u_a	nondimensional apparent radial velocity
u_c	correction to u
v	nondimensional induced azimuth velocity
v_s	nondimensional velocity introduced in Eq. (II-3)
v_c	correction to v
w	nondimensional induced axial velocity
w_a	nondimensional apparent axial velocity
w_c	correction to w
w(x)	nondimensional induced axial velocity distribution at blade
x	nondimensional radial coordinate
x*	integration variable, x
X	coordinate in Figure 1
Y	coordinate in Figure 1
z	nondimensional axial coordinate
z*	integration variable, z
Z	axial coordinate
α	sectional angle of attack

β	radial pitch angle of the helix
Γ	circulation strength of the tip vortex
$\Gamma(x)$	circulation distribution at the blade
δ	the arc element, Eq. (III-4)
ϵ	nondimensional core radius
λ	exponent in the equation (III-1)
ρ	air density
σ	rotor solidity
θ	blade pitch angle, constant in this analysis
ϕ	axial pitch angle of the helix
ψ	azimuth coordinate
ψ^*	integration variable,
Ω	blade angular velocity

Subscripts

c	due to the core
e	effective
i	induced
r	radial
s	subscript in v_s in the Eq. (II-3)
z	axial
ψ	azimuth
∞	ultimate wake

LIST OF ILLUSTRATIONS

SUMMARY

The success of the blade element theory in the performance analysis of hovering rotors depends greatly upon the accurate specification of the geometry of the vortex wake, particularly in the near wake. The use of experimentally observed geometry produces excellent results, but, completely theoretical analyses fail to achieve similar success since the theoretically calculated geometry does not contract and move down rapidly enough. In this analysis efforts are made to locate the cause of the discrepancies and an approach is suggested to reduce or eliminate them.

The velocity in the blade fixed reference system at a point on a vortex filament must be tangential to the vortex filament referred to the same system. This is called the consistency requirement and is developed in this analysis in terms of the apparent velocity components. It is shown that the apparent velocity components calculated from a given vortex system using the Biot-Savart law do not satisfy these consistency requirements. This is because the Biot-Savart law has inherent singularities when the point of interest lies on the vortex filament itself. Therefore, the velocity due to a small region in the vicinity of a point on the filament cannot be calculated directly. However, it is

known that the Biot-Savart law can be used to calculate the effect of the same vortex system at the blade very accurately. The discrepancies in the induced velocity calculated in the wake are, therefore, thought to be the local effects of this small region and are then called the core effects. No model of the tip vortex core that will completely account for the effects of the core exists presently. Therefore, the effects of the core are incorporated into the analysis semi-empirically by modifying the velocity components in the wake.

With these suggested modifications, it is shown that the consistency requirements are satisfied more closely for rotors with one to four blades operating at various thrust levels. A six bladed rotor was considered but the computations could not be completed because of very strong interaction between the tip vortex and the blade. It is concluded that the core effects suggested can be used effectively to improve the calculated geometry of the tip vortex.

CHAPTER I

INTRODUCTION

Previous Research

Performance Prediction and Vortex Wake

Past research in the field of performance prediction of a helicopter rotor indicates that the predicted performance is as accurate as the inflow calculations at the rotor disc. With accurate knowledge of the inflow distribution at the rotor, it is possible to calculate blade loading and total thrust and torque using the blade element theory. The actuator disc theory [1] provides a good starting point but is not satisfactory for final performance analyses of modern rotors. The improvements in the performance prediction due to the combined momentum and blade-element theory are considerable. However, the vortex wake analyses provide much better results. The use of the complex wake models [2] was possible only with the advent of the high speed digital computers.

For a hovering rotor, the vortex wake can be divided into two regions which may be defined as the near wake (about one diameter down the wake) and the far wake. The

accurate specification of the near wake geometry is very essential to the accuracy of the inflow calculation and the overall analysis [2,3,4,5].

Prescribed Vortex Wake Models in Hovering

The present analysis restricts itself to the hovering regime. This simplifies the analysis considerably as the time dependent blade loadings associated with forward flight need not be considered. Also, hovering out of ground effect is an important performance criterion and is used for evaluation purposes [3]. The first vortex wake analysis for propellers in axial flight was developed by Goldstein [6]. His wake model includes a set of semi-infinite, equidistant, co-axial, helicoidal surfaces representing the vortex sheet shed from the trailing edge of each blade. The analysis neglects slipstream rotation and applies rigorously only to optimum and lightly loaded propellers in axial flight. Lock [7] extended the theory to the hovering condition for a helicopter rotor. In spite of the limitations of an unrealistic noncontracting wake, the Goldstein-Lock blade-element analysis represented the state of the art until recently [2].

Gray [8] developed a model of the wake for a single-bladed rotor to analyse the motion of the tip vortex. His ultimate wake model consisted of a constant diameter, constant axial pitch, helical tip vortex with a solid-body rotation core. The tip vortex strength is calculated by

relating it to the wake induced influence coefficients and the geomtry in the ultimate wake. Gray [8,9] further performed flow vizualization experiments and measured the tip vortex geometry for the single-bladed rotor. The observed tip vortex geometry is a contracting helix that approaches a constant diameter and a constant axial pitch as it moves down the wake. He used the observed tip vortex geometry and the tip vortex strength calculated in the ultimate wake to calculate the induced downwash at the blade, the aerodynamic loading, and the total thrust. This was the first effort of its kind where the observed geometry of the vortex wake was used. The calculated total thrust in this analysis matched well with the observed value.

Landgrebe [4] developed a prescibed wake analysis that uses the observed wake geometry. The entire wake consists of a number of filaments shed at the trailing edge of the blade. A certain number of outer filaments are immediately rolled into a tip vortex with a solid core. The strength of the filaments and the tip vortex is not known at the outset but is calculated in an implicit procedure by relating the filament strength and the induced influence coefficients to the discretized blade circulation distribution. The procedure also yields the blade loading which is integrated to get the total thrust. Landgrebe also performed a considerable number of flow vizualization experiments in order to obtain a range of tip vortex and

sheet geometry data. The results of the prescribed wake analysis using the observed geometry are in very good agreement with the observed performance.

Theoretically Calculated Vortex Wake Models

The elaborate experiments required to obtain the geometry of the vortex wake led to the development of methods to calculate the wake geometry theoretically [4]. A starting geometry, usually a constant diameter type, and a circulation distribution are prescribed. The velocity induced by the prescribed geometry is then calculated at certain points on the vortex elements. The wake vortex elements are then released and allowed to displace for a short time under the influence of this velocity field. This new geometry is used to calculate a new velocity field and the next displacement. The iterations are continued until the change in geometry between the successive stages is small. This geometry is used as input into the prescribed wake analysis to get the new blade circulation distribution. This distribution is then used to calculate a new geometry by following a similar procedure as described above. The calculations are stopped when both the geometry and the total thrust converge to an acceptable solution. The computer time required for such calculations is usually large and some simplifications in the calculations are introduced in order to reduce the computer time. The tip vortex geometry at the end of such a procedure however, does

not match with the experimentally observed geometry especially in the near wake.

Gray and Brown [5] used the ultimate wake concept and developed a method of calculating the geometry of the tip vortex and the inboard sheet elements for a single-bladed rotor. In their approach the most dominant element, the tip vortex, is considered first and then the less dominant elements, the sheet filaments, are introduced. The procedure involves iterations on the velocity field and the displaced geometry as the sheet elements are introduced one by one. The tip vortex strength coefficient is calculated such that the calculated tip vortex geometry matches with the observed geometry in the ultimate wake. The tip vortex geometry in the near wake, however, does not match with the observed.

The Discrepancies

The results of the theoretical analyses show that the tip vortex does not move down the wake or contract rapidly enough. This is due to the fact that the induced velocity calculated in the wake is too small, even when the observed geometry is used as the input.

In these analyses, the Biot-Savart law is used to calculate the induced flow field, both at the blade and in the wake. The induced velocity calculated at the blade is quite accurate but the wake velocity is in error. This is due to the fact that the integration in the Biot-Savart law

is terminated at a small interval on either side of the point of interest when the point of interest lies on the vortex filament because of an inherent singularity. This singularity does not exist when the point is away from the filament. The interval over which the integration is not performed is small and its effect on the induced velocity components is neglected or included only partially, e.g., its effect in the axial direction is calculated using the solid-body rotation model [5]. The effect of this interval in the radial and azimuthal directions may be significant. A model of the core that completely accounts for the effects of this interval, termed as the core effects, is not available presently. In this analysis, the core effects are introduced into the analysis semi-empirically by modifying the velocity components. It is shown that the corrected velocity components are consistent and the calculated geometry agrees well with the experiment.

Definition of the Problem

The aims of the analysis are:

1. To develop the general consistency relations using the procedure of Ref. 5;

2. With the observed geometry as an input, to point out the discrepancies between the induced and empirically derived apparent velocity and the calculated and observed geometry using the existing procedure. (Case 1 of this

analysis);

3. To modify these consistency relations using two corrections and to recalculate the apparent velocity and geometry. (Cases 2 and 3);

4. To identify these corrections as the effects of the core in the individual directions (Case 2 in the axial direction, and Case 3 in the radial direction) by demonstrating the self-preservedness of the tip vortex geometry under the influence of the induced apparent velocity. It is noted here that when such an approach is taken, a physical inconsistency of having different azimuth components in the two corrections is introduced; and

5. To resolve the inconsistency stated in 4 above in a manner such that the corrections introduced in the analysis can be recognised as the corrections to the azimuth and radial components of the actual velocity in the wake.

Chapter II presents the velocity displacement model. The developments described in 5 above are presented in Chapter II even though they took place after the complete calculations were performed. Chapter III describes the wake vortex system and the computation procedure. The results are discussed in Chapter IV. Conclusions and recommendations are presented in Chapter V.

CHAPTER II

VELOCITY DISPLACEMENT MODEL

The consistency relations between the geometry of a vortex filament and the wake induced velocity are developed initially using the same general procedure as Ref. 5. The apparent velocity concept is then introduced. The hypothesized effects of the core are incorporated into the apparent velocity which is used to calculate the displacements and the new geometry. Two cases of correction to the tip vortex motion are presented in addition to the one without correction.

Consistency Requirement

The coordinates and the velocity components are referenced in a blade fixed system shown in Figure 1. Such a description makes the flow field and the geometry of the vortex filament constant in time and requires that the line describing the vortex filament also be a streamline in that reference system. This is the requirement that makes the velocity field consistent with the geometry of the vortex filament. In terms of the geometry of a helical filament, the consistency requirement can be developed from the

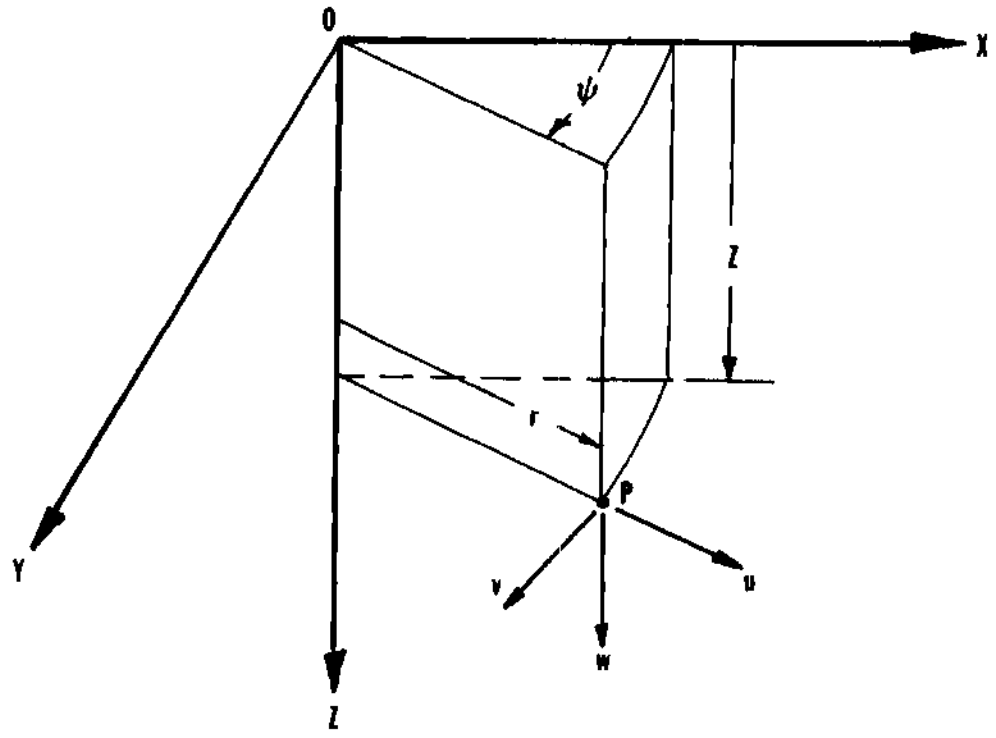

Figure 1. Reference System for the Coordinates and Velocity Components

velocity diagrams shown in Figure 2a and is described by the following equations:

$$\tan\beta = \frac{1}{x}\frac{dx}{d\psi} = \frac{u}{v_s + v} \qquad \text{(II-1a)}$$

and

$$\tan\phi = \frac{1}{x}\frac{dz}{d\psi} = \frac{w + w_c}{v_s + v}. \qquad \text{(II-1b)}$$

where β and ϕ are the radial and axial pitch angles which are related to the local tangent, x and z are the radial and axial coordinates which can be parametrically expressed in termes of ψ, the azimuth coordinate, u, v, w are the velocity components induced by the external vortex field, w_c is the axial component calculated using the solid body rotation model to be described later, and v_s is the azimuth component that includes the blade relative motion, x/c_T, and the core effect in the azimuth direction.

Apparent Velocity Concept

In determining the motion of the vortex filament, the usual practice is to identify a number of points along the vortex so that their displacement in the theoretical flow field adequately defines the vortex geometry as time progresses. The displacement and the three coordinates that

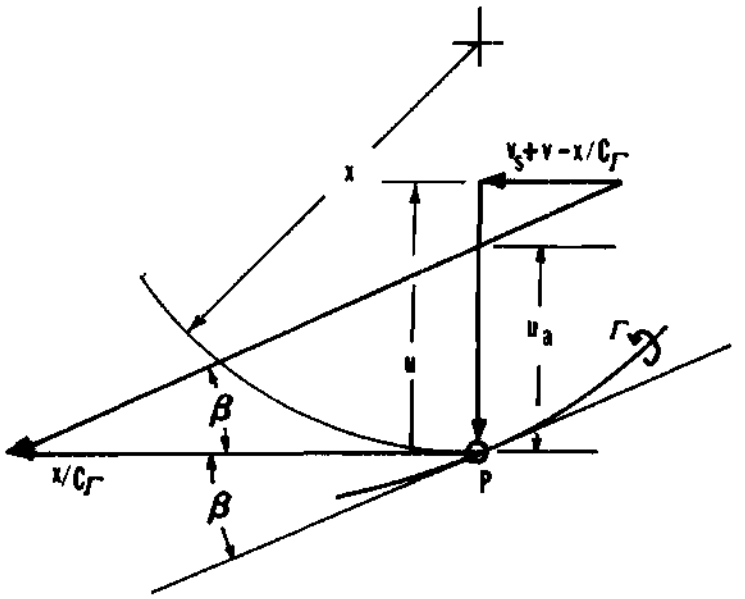

i) Radial pitch angle and apparent velocity component

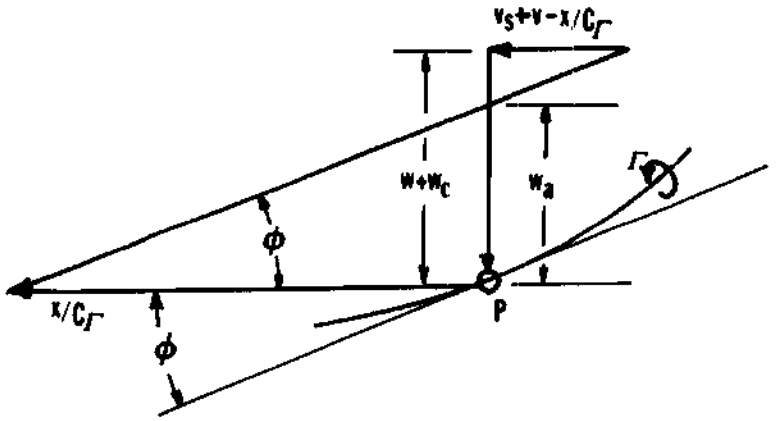

ii) Axial pitch angle and apparent velocity component

Figure 2a. Velocity Diagrams in the Wake.

define it will vary with time. In the experiments, however, it is convenient to observe the motion of the point of intersection of the vortex filament with the radial plane. This motion is called the apparent motion. The velocity components that correspond to such motion are called the apparent velocity components and are given by

$$u_a = \frac{x}{c_\Gamma} \tan\beta = \frac{1}{c_\Gamma} \frac{dx}{d\psi} = \frac{u}{v_s + v} \frac{x}{c_\Gamma} \qquad \text{(II-2a)}$$

and

$$w_a = \frac{x}{c_\Gamma} \tan\phi = \frac{1}{c_\Gamma} \frac{dz}{d\psi} = \frac{w + w_c}{v_s + v} \frac{x}{c_\Gamma}. \qquad \text{(II-2b)}$$

There are only two components of the apparent velocity once the radial plane of interest is specified. The velocity diagrams illustrating the individual radial and axial apparent velocity components are shown in Figures 2a (i), drawn in the Z plane, and 2a (ii), drawn in the tangent plane. Along with the radial plane, these two planes form a regular trihedron relative to the point, P. The component, x/c_Γ, which is common to both the figures is perpendicular to the radial plane and is the third component of the apparent motion, and therefore, the advancement of the azimuth coordinate can be directly related to the advancement of time. The motion of the tip vortex now can

be studied in a certain number of fixed radial planes. Note that the third members of the Eqs. (II-2) are empirically derived from the observed geometry by differentiating the geometry with respect to ψ. The extreme right members of these equations are the apparent velocity components in terms of the computed velocities. The consistency of the flow field will then be satisfied if the apparent velocity components induced by the vortex wake are equal to those empirically derived from the observed geometry. The geometry of a filament will remain unchanged with the passage of time only if Eqs. (II-2) are satisfied at all points on the filament.

Superimposed Blade Motion, v_s

The quantity v_s in the above expressions will now be considered in detail. In the previous analyses, [4,5], v_s was equal to x/C_Γ. The effects of the core which have been neglected in these analyses, are here combined with the blade relative motion, x/C_Γ, into v_s, and it is found that a general first approximation for v_s can be given by

$$v_s = \frac{Qx^i}{C_\Gamma}. \qquad \text{(II-3)}$$

where i is a variable exponent and Q is a parameter calculated during the analysis such that the Eqs. (II-2)

are satisfied in both the near and the ultimate wake.

The Three Cases

Three different cases for v_s having different values for i are now considered. In the first case, i=1 and Q=1. This is the case in which v_s is simply the blade relative motion, x/c_Γ, and no core correction is applied. In the other two cases with i=0 and i=-1, Q is calculated during the analysis. In these cases, v_s is different from the blade relative motion and includes a different core correction in each case. The effect of these corrections on the expressions for v_s and the apparent velocity components is described below.

Case 1: i=1 and Q=1.

This results in the expressions developed in Ref. 5. The v_s here is simply the blade rotational velocity and takes the form

$$v_s = \frac{x}{c_\Gamma} \qquad \text{(II-4)}$$

and Eqs. (II-2) become

$$u_a = \frac{1}{c_\Gamma}\frac{dx}{d\psi} = \frac{u}{1+vc_\Gamma/x} \qquad \text{(II-5a)}$$

and

$$w_a = \frac{1}{C_\Gamma}\frac{dz}{d\psi} = \frac{w+w_c}{1+vC_\Gamma\sqrt{x}}. \qquad \text{(II-5b)}$$

Equation (II-5a) is identically satisfied in the ultimate wake since both $dx/d\psi$ and u are zero there. In the ultimate wake, Eq. (II-5b) becomes

$$C_\Gamma = \frac{(dz/d\psi)_\infty}{w_\infty + w_{c_\infty} - v_\infty (dz/d\psi)_\infty}. \qquad \text{(II-6)}$$

In Ref. 5, this equation has been used to calculate the strength, C_Γ, of the tip vortex. With this value of C_Γ, the induced apparent velocity componets are less than the empirically derived values. Therefore, the geometry calculated from the induced velocity has a contraction rate and axial pitch angle which are too small in the near wake.

Case 2: i=0

Here, Q is unknown and v_s takes the form

$$v_s = \frac{Q}{C_\Gamma} \qquad \text{(II-7)}$$

and Eqs. (II-2) yield

$$u_a = \frac{1}{C_\Gamma}\frac{dx}{d\psi} = \frac{u}{Q/x+vC_\Gamma\sqrt{x}} \qquad \text{(II-8a)}$$

and

$$w_a = \frac{1}{C_\Gamma}\frac{dz}{d\psi} = \frac{w+w_c}{Q/x+vC_\Gamma\sqrt{x}}. \qquad \text{(II-8b)}$$

In the ultimate wake Eq. (II-8b) takes the form

$$Q = \frac{C_\Gamma\,[w_\infty+w_{c_\infty}-v_\infty(dz/d\psi)_\infty]}{(dz/d\psi)_\infty}. \qquad \text{(II-9)}$$

The C_Γ in Eq. (II-9) is equal to the value of the strength of the tip vortex at the tip and is determined by the amount of vorticity shed into the wake from the blade outboard of the point where $C_\Gamma(x)$ is maximum. Hence C_Γ is simply $C_\Gamma(x)_{max}$. $C_\Gamma(x)_{max}$ can be calculated using the procedure presented in Chapter III for the given tip vortex geometry. Q can be calculated from Eq. (II-9).

Once the value of Q is known, Eqs. (II-8) can be used to compare the empirically derived and induced apparent velocity components. The v_s used here is a constant. It will be demonstrated, through calculations, that the effect of this modification is to improve the comparison of the induced and empirically derived axial apparent velocity in Eq. (II-8b).

Case 3: $\lambda=1$

This case results in

$$v_s = \frac{Q}{x C_\Gamma}, \qquad \text{(II-10)}$$

$$u_a = \frac{1}{C_\Gamma}\frac{dx}{d\psi} = \frac{u}{Q/x^2 + v C_\Gamma/x}, \qquad \text{(II-11a)}$$

and

$$w_a = \frac{1}{C_\Gamma}\frac{dz}{d\psi} = \frac{w+w_c}{Q/x^2 + v C_\Gamma/x}. \qquad \text{(II-11b)}$$

Equation (II-11b) reduces to Eq. (II-9) in the ultimate wake since x=1 for a fully contracted tip vortex. This means that the same value of Q is obtained in both Cases 2 and 3. This Q can be used to compare the induced apparent velocity components with the empirically derived. The v_s in this case varies inversely as the radial coordinate. It will be demonstrated that this type of correction improves the comparison of the induced and empirically derived radial apparent velocity in Eq. (II-11a).

Geometric Displacements

In a theoretical method, the new geometry is calculated from the velocity field induced by the earlier

geometry. Given the induced apparent velocity calculated from the analysis, the displacements can be calculated by integrating the apparent velocity with respect to ψ using the following equations:

$$\Delta x = u_a \Delta\psi C_\Gamma \qquad \text{(II-12a)}$$

and

$$\Delta z = w_a \Delta\psi C_\Gamma . \qquad \text{(II-12b)}$$

Identification of the Core Effects

It is noted here that in order for these corrections to be used effectively in a theoretical analysis, one correction from Case 2 and the other from Case 3 have to be used together. This approach introduces an inconsistency into the problem, namely, the azimuth components of the actual velocity used in the calculation of the apparent velocity components are different in the near wake. This inconsistency could not be resolved until after the results were calculated. It then was noticed that the term vC_Γ/x in the denominators of the third members of Eqs. (II-11a) and (II-8b) is two orders of magnitude smaller than the other terms such as Q/x and Q/x^2. If vC_Γ/x is neglected, the expressions for the induced apparent velocity can be rewritten as

$$u_a = \frac{u}{Q/x^2 + vC_\Gamma/x} \simeq \frac{ux}{Q/x} \qquad \text{(II-13a)}$$

and

$$w_a = \frac{w+w_c}{Q/x + vC_\Gamma/x} \simeq \frac{w+w_c}{Q/x}. \qquad \text{(II-13b)}$$

The denominators are now the same for both components. The Q/x term is the result of the correction in Case 2. Also the numerator of Eq. (II-13a) is now ux instead of u as in Eq. (II-11a). The corrections to the individual components in the azimuth and radial directions, v_c and u_c, can now be defined with the help of Eqs. (II-13). They are

$$v_c = \frac{x}{C_\Gamma}\left(\frac{Q}{x} - 1\right) \qquad \text{(II-14)}$$

and

$$u_c = u\,(x - 1) \qquad \text{(II-15)}$$

The correction to the radial component, u_c, vanishes in the ultimate wake since x -> 1 and u -> 0. The correction in the azimuth direction, v_c, vanishes in the ultimate wake if Q=1. If Q is not equal to unity then the v_s is such that it matches $C_\Gamma(x)_{max}$ and C_Γ in the ultimate wake.

The Eqs. (II-14) and (II-15) give two corrections to

the two components of the actual velocity in the wake. If w_c is recognised as the core contribution in the axial direction calculated from the solid-body rotation model presented in Ref. 5, then there is a contribution due to the core in each of the three directions, namely, u_c (radial), v_c (azimuth), and w_c (axial). The apparent velocity components u_a and w_a can now be calculated using these components, u_c, v_c, and w_c , along with the induced velocity calculated from the external vortex field, (u,v,w), and the superimposed blade motion, x/C_Γ. The velocity diagrams that include these components are shown in Figure 2b and the resulting expressions, equivalent to (II-1), are given by the following:

$$\tan\beta = \frac{1}{x}\frac{dx}{d\psi} \cong \frac{u+u_c}{x/C_\Gamma + v_c} \qquad \text{(II-15a)}$$

and

$$\tan\phi = \frac{1}{x}\frac{dz}{d\psi} \cong \frac{w+w_c}{x/C_\Gamma + v_c}. \qquad \text{(II-15b)}$$

Due consideration should be given to the fact that the above equations do not contain v since it is neglected.

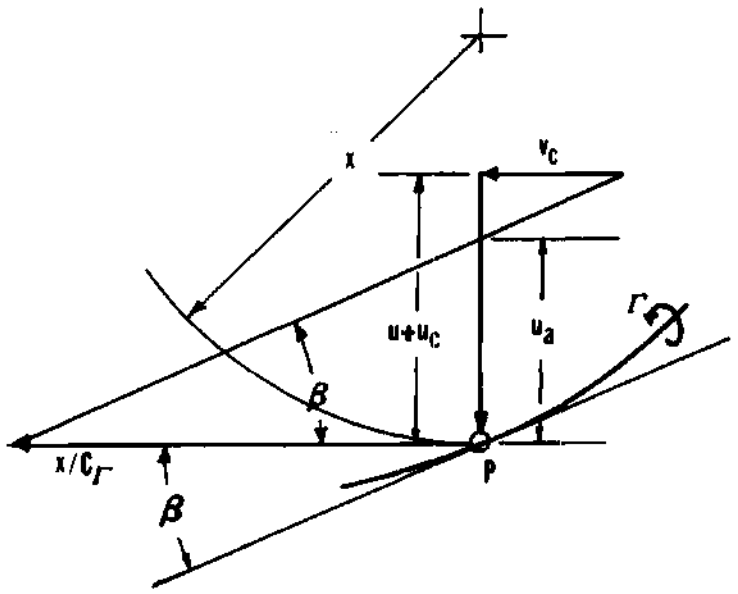

i) Radial pitch angle and apparent velocity component

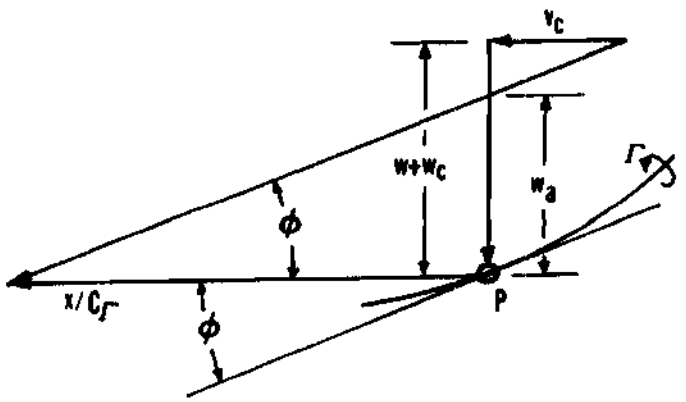

ii) Axial pitch angle and apparent velocity component

Figure 2b. Velocity Diagrams in the Wake with u_c, v_c, w_c Identified.

CHAPTER III

DESCRIPTION OF THE WAKE AND COMPUTATION PROCEDURE

In this chapter, the wake vortex system is described. The procedure to calculate the strength of the vortex elements and the Biot-Savart expressions to calculate the induced velocity at a given point due to these elements are presented.

Wake Vortex System

The wake of a single bladed helicopter rotor in hovering flight [8] is illustrated in Fig. 3. The essential elements of the wake system for a single-bladed rotor wake simply repeat for a multibladed rotor. These elements are: the tip vortex, the vortex sheet, and the blade bound vortex.

The Tip Vortex

The tip vortex is the strongest of all the elements and is shed from the tip of the blade. It has a contracting helical shape and a finite core. The centerline of this filament can be mathematically approximated by the following equations as determined from experiments [8]:

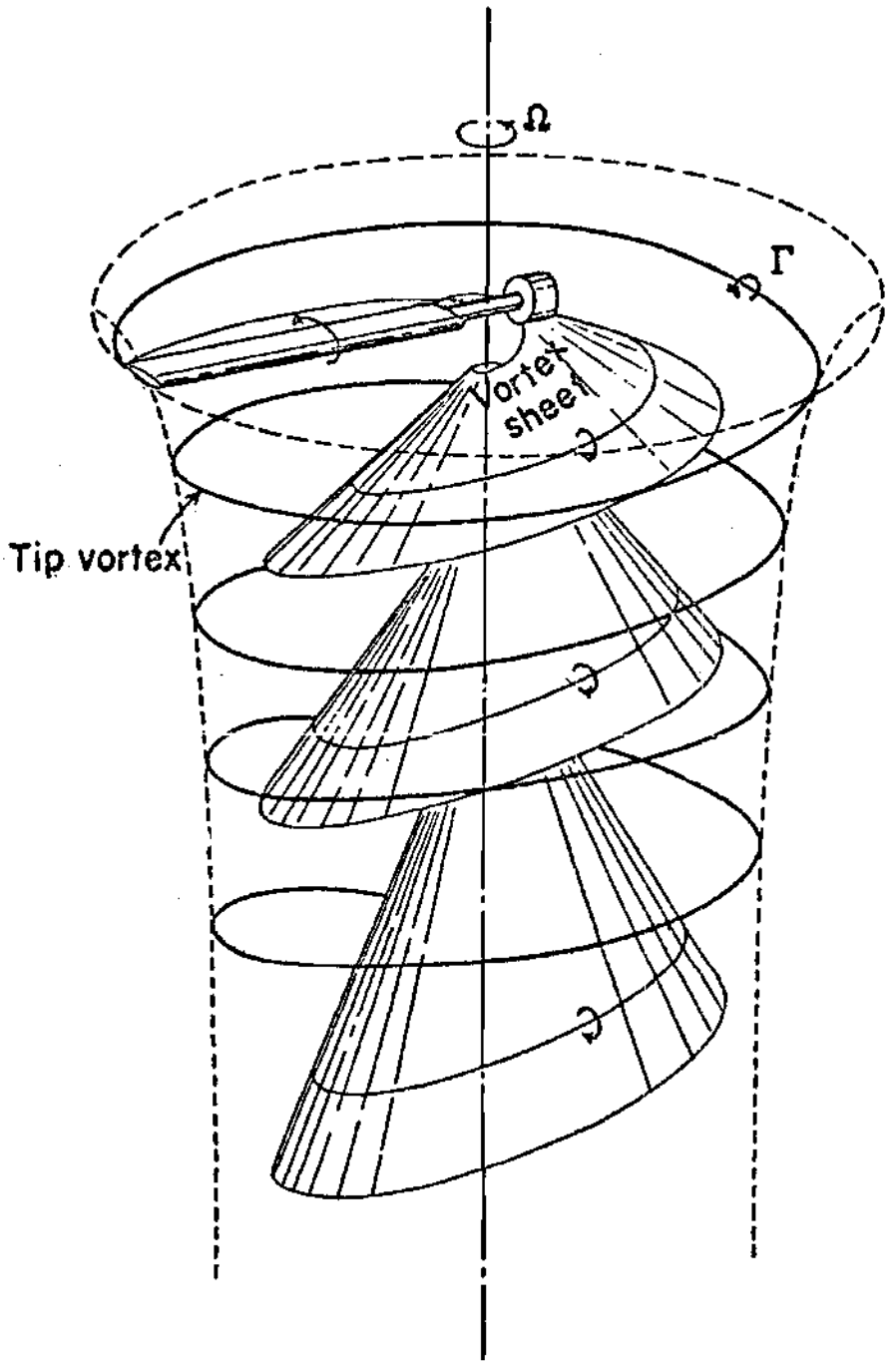

Figure 3. Schematic of the Wake Vortex System.

$$x = \frac{r}{RA} = 1 + \frac{(1-A)}{A} e^{-\lambda\psi}, \qquad \text{(III-1)}$$

$$z = \frac{Z}{RA} = \frac{k_1\psi}{A}, \qquad 0<\psi<\frac{2\pi}{b}, \qquad \text{(III-2a)}$$

or

$$z = \frac{Z}{RA} = \frac{k_1 2\pi}{Ab} + \frac{k_2}{A}\left(\psi - \frac{2\pi}{b}\right), \quad \psi<\frac{2\pi}{b}. \qquad \text{(III-2b)}$$

These equations are written in a blade reference system. The ψ is the wake azimuth coordinate and x and z are the radial and axial coordinates nondimensionalized with respect to RA, the radius of the tip vortex in the ultimate wake. A and λ are the contraction parameters and k_1 and k_2 are the axial displacement parameters. A, λ, k_1 and k_2 are constant for a given rotor at a given thrust level. $2\pi/b$ is the azimuth location at which the next following blade passes over the tip vortex.

The core radius, ϵRA, and the circulation strength of the tip vortex, C_Γ, are assumed to be constant down the wake. A typical blade circulation distribution peaks very close to the blade tip and goes to zero at the tip quite abruptly. All of the positive vorticity shed from the blade tip into the wake rolls up into the tip vortex. The strength of the tip vortex is, therefore, the same as the

peak value of the blade circulation distribution, $C_\Gamma(x)$. The calculation of $C_\Gamma(x)$ requires an iterative procedure that is presented later in this chapter.

The Sheet of Vorticity

The vorticity shed inboard of the point where the circulation distribution is maximum forms the inner sheet. This portion of the wake has been observed in the experiments but has not been as well defined as the tip vortex [7]. The outer portions of the sheet have been observed to travel down the wake faster than the inner portions and hence the sheet takes the approximate conical shape that is apparent in Fig. 3. The sheet of vorticity also appears to remain entirely within the tip vortex envelope. The geometry of the sheet is calculated during the analysis in a way that will conform with the observed shape. The actual sheet of vorticity is a surface of discontinuity and the application of the Biot-Savart law to the sheet is very difficult because of its three dimensional and irregular shape. Hence the sheet is redistributed into a number of filaments of equal strength, each representing part of the vorticity shed into the wake inboard of the point of $C_\Gamma(x)_{max}$. The geometric locations of the origins of the filaments are determined from the circulation distribution, $C_\Gamma(x)$, along the blade using the following procedure. The first point on the blade is located such that the amount of circulation shed into the wake between

the point of maximum $C_f(x)$ and this point is equal to the strength selected for each filament. The origin of the outermost filament which will represent the vorticity shed between these two points is placed at the center of this interval. The second such interval is located in a similar manner and its center becomes the origin of the second sheet filament. The process is repeated until all of the filaments are accounted for and their origins at the blade are known. The z coordinate of the filament is calculated by integrating the axial component of the induced velocity starting at the origin of the filament and marching down the wake in the azimuth direction. The x coordinate of the filament is forced to be proportional to the x coordinate of the tip vortex at the corresponding z plane in order to keep the filament within the tip vortex envelope. The geometries of all of the filaments in the wake are not calculated since such a scheme would require a large amount of computer time. Only the geometry of the outermost filament is calculated in its entirety. The points on the inner filaments are made to lie on a line joining the point on the outer filament and the origin in the given radial plane. The relative spacing of the filaments is made proportional to the relative spacing of the origins of these filaments at the blade. This makes the surface on which the filaments lie conical as observed. The geometry of the filaments thus calculated is used to calculate the induced velocity at the tip vortex.

Since the points on the tip vortex lie outboard of the filaments, the error in the calculation of the induced velocity is expected to be small.

The Bound Vortex

This is the vortex that replaces the blade and runs from the root to the tip of the blade. The strength of this vortex is the blade circulation distribution, $C_\Gamma(x)$. The self-induced effect of this straight element is zero but its effect at any other point may be appreciable.

Computational Procedures

Calculation of Blade Circulation and Loading

The strength of the tip vortex, the bound vortex, and the sheet filaments depend on $C_\Gamma(x)$ which is not known initially. The blade downwash distribution which is needed to calculate the blade circulation distribution depends on the geometry and strength distribution in the wake. Hence, the calculation of $C_\Gamma(x)$ is accomplished by an iterative process. This procedure is also used to calculate the thrust loading for a given tip vortex geometry and is as follows:

a. Calculate the nondimensional induced downwash distribution, w(x), at the blade using the tip vortex alone;

b. Calculate C_Γ in the ultimate wake for this geometry from Eq. (II-6) and use this value of C_Γ as the starting value;

c. Using the w(x) and the blade and airfoil characteristics, calculate the induced angle of attack, the effective angle of attack, the local lift coefficient, the thrust loading, and the blade circulation distributions using the following equations:

$$\alpha_i(X) = \frac{w(x)C_\Gamma}{x}, \qquad \text{(III-3)}$$

$$\alpha_e(x) = \theta - \alpha_i(x), \qquad \text{(III-4)}$$

$$c_l(x) = a\alpha_e(x), \qquad \text{(III-5)}$$

$$\frac{dC_T(x)}{dx} = \frac{\sigma}{2b}(xA)^2 A\, a\left[\theta - \frac{w(x)C_\Gamma}{x}\right], \qquad \text{(III-6)}$$

$$C_\Gamma(x) = \frac{\sigma}{8b}(xA)\, a\left[\theta - \frac{w(x)C_\Gamma}{x}\right]; \qquad \text{(III-7)}$$

d. Determine $C_\Gamma(x)_{max}$, set $C_\Gamma = C_\Gamma(x)_{max}$, and repeat step c until consecutive values of $C_\Gamma(x)_{max}$ exhibit satisfactory convergence;

e. Using $C_\Gamma(x)$, set up the sheet origins, calculate the sheet geometry, calculate the downwash at the blade due to the sheet, and add this to w(x);

f. Go to step c.

The calculations are terminated when the value of $C_\Gamma(x)_{max}$ calculated using the sheet contribution converges.

Since the sheet computations take up a lot of computer time, a compromise between the accuracy of the sheet geometry and computer time is established.

Calculation of Induced Velocity in the Wake

When the previous calculations are terminated, the actual performance calculations are also complete. At this point, all of the input (the tip vortex, the sheet of vorticity, and the bound vortex) required to calculate the induced velocity at the tip vortex are available.

The induced velocity components due to the tip vortex at a given point (ψ,x,z) can be calculated from the Biot-Savart law as follows

$$u=\int\left\{\frac{dz^*}{d\psi^*}x\sin(\psi^*-\psi)+\left[\frac{dx^*}{d\psi^*}\sin(\psi^*-\psi)+x\cos(\psi^*-\psi)\right](z-z^*)\right\}\frac{d\psi^*}{\rho^{*3}}$$

$$v=\int\left\{\frac{dz^*}{d\psi^*}\left[x-x^*\cos(\psi^*-\psi)\right]-\left[\frac{dx^*}{d\psi^*}\cos(\psi^*-\psi)-x\sin(\psi^*-\psi)\right](z-z^*)\right\}\frac{d\psi^*}{\rho^{*3}}$$

$$w=\int\left\{x^{*2}-xx^*\cos(\psi^*-\psi)-x^*\frac{dx^*}{d\psi^*}\sin(\psi^*-\psi)\right\}\frac{d\psi^*}{\rho^{*3}} \qquad \text{(III-8)}$$

where $\rho^{*2}=x^2+x^{*2}-2xx^*\cos(\psi^*-\psi)+(z-z^*)^2$.

The primed quantities in the these expressions are the integration variables and are calculated from Eqs. (III-1) and (III-2). Equations (III-8) are derived from the more general expressions given in Ref. 10. The velocity in

this analysis is nondimensionalized with respect to $(\Omega R A C_f)$. It is immediately evident from Eqs. (III-8) that the integrands are singular if the point of interest (ψ, x, z) lies on the vortex filament itself. The singularity is avoided by eliminating the integration from $(\psi-\delta)$ to $(\psi+\delta)$ where δ is obtained from

$$\delta = \arctan \frac{\sqrt{\epsilon(x-\epsilon)}}{x}. \qquad \text{(III-9)}$$

This formula can be established from Fig. 4. The missing contribution to the axial component due to the element between $(\psi-\delta)$ and $(\psi+\delta)$ is calculated from

$$w_c = \frac{1}{x}\left\{\ln\left(\frac{8x}{\epsilon}\right) - .25 - \ln\left[\cot\left(\frac{\delta}{4}\right)\right]\right\} \qquad \text{(III-10)}$$

which is a simplified form of a similar expression developed in Ref. 5. The radial and azimuthal contribution from this element are considered to be negligible. The contribution due to all of the tip vortices in a multi-bladed case is obtained by simply adding the contributions from the individual tip vortices. Eq. (III-10) is used in the calculations for only one of the tip vortices.

In order to calculate the induced velocity due to the sheet, the filaments are broken into straight line segments

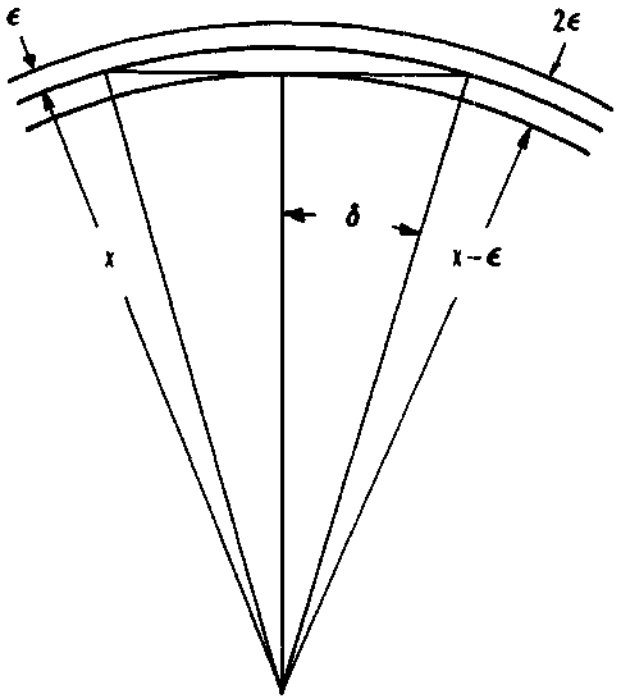

Figure 4. Cutoff Angle δ.

that run from one radial plane to another. The Biot-Savart law is applied to these straight segments. The total contribution is calculated by adding the contributions of all of the segments of all the filaments. This is accomplished by using an algorithm presented in Ref. 4.

The contributions due to the blade bound vortex are given by

$$u = \int C_{\Gamma}(x)\, z\, \mathrm{Sin}(\psi^{*}-\psi)\, \frac{dx^{*}}{\rho^{*3}}$$

$$v = -\int C_{\Gamma}(x)\, z\, \mathrm{Cos}(\psi^{*}-\psi)\, \frac{dx^{*}}{\rho^{*3}} \qquad \text{(III-11)}$$

$$w = -\int C_{\Gamma}(x)\, x\, \mathrm{Sin}(\psi^{*}-\psi)\, \frac{dx^{*}}{\rho^{*3}}$$

where $\rho^{*2} = x^2 + x^{*2} - 2xx^{*}\,\mathrm{Cos}(\psi'-\psi) + z^2$.

Comparison for Consistency Requirement

The incuced velocity due to all of the elements is calculated at certain locations on the tip vortex. This induced velocity distribution down the wake is used in Eqs. (II-5) to show the discrepancies that have been noted. Then the final value of $C_{\Gamma}(x)_{max}$ is used in Eq. (II-9) to calculate a value of Q. The induced and empirically derived apparent velocity components are then calculated and compared with each other. After the apparent velocities are

calculated, the next geometry of the tip vortex is calculated by successive application of Eqs. (II-12). The following expressions result:

$$x_{n+1} = x_n + .5\,(u_{a_{n+1}} + u_{a_n})\,C_\Gamma\,(\psi_{n+1} - \psi_n) \qquad \text{(III-12a)}$$

and

$$z_{n+1} = z_n + .5\,(w_{a_{n+1}} + w_{a_n})\,C_\Gamma\,(\psi_{n+1} - \psi_n) \qquad \text{(III-12b)}$$

The starting point for these equations is taken to be the tip. The geometry of the tip vortex thus calculated is compared with the observed geometry of the tip vortex. The results are discussed in the next chapter.

Numerical Implementation

The computational procedures described above were translated into a Fortran IV program with four segments:

1. Induced downwash,
2. Circulation distribution and the sheet geometry,
3. Induced velocity at the tip vortex,
4. Apparent velocity and displaced geometry.

A fifth program was developed to plot the data on a Calcomp digital plotter. For the integrals where the integrands are known, as in the cases of Eqs. (III-8) and (III-11), the Romberg integration technique was used. The number of iterations performed on the sheet geometry is decided by the computer time required. The number of filaments used to

represent the sheet is decided by the slope of the $C_T(x)$ curve; the greater the slope of the curve, the more the number of filaments. Simple integrations, such as the thrust and geometry integrations, are performed using the trapezoidal rule. The program can be run continuously. However, for blade numbers higher than two, the segments were run separately in order to be sure of the intermediate results. The programs were executed on a CDC 6400 computer housed in the Rich Electronic Computing Center of the Georgia Irstitute of Technology.

CHAPTER IV

DISCUSSION OF RESULTS

The computational procedures described in Chapter III are performed for one-, two-, three- and four-bladed rotors. An attempt was made to perform calculations for a six-bladed rotor but the efforts were abandoned because of certain difficulties. The following table presents geometric data and calculated values of Q for the conditions of rotors considered:

No	b	C_T	θ	A	λ	k_1	k_2	Q
1	1	.00195	6.5	.746	.160	.0218	.0420	1.15
2	1	.00280	8.5	.733	.164	.0280	.0490	1.15
3	1	.00370	10.1	.722	.177	.0338	.0569	1.11
4	2	.00193	6.0	.780	.197	.0138	.0439	1.05
5	2	.00280	8.0	.780	.221	.0200	.0529	.95
6	2	.0035	10.1	.780	.239	.0250	.0592	.96
7	3	.00220	6.0	.780	.190	.0150	.0470	1.36
8	3	.00320	8.0	.780	.225	.0191	.0560	1.22
9	4	.00371	8.0	.780	.245	.021	.06	1.45

The conditions are numbered for convenient reference in the text. The results for the nine conditions show a number of similarities and the example of Condition No. 2 is typical of these. The results for all the cases (1 through 3) are presented only for Condition No. 2. For the other conditions, Case 1 is presented in one figure and the individual effects of the corrections in Cases 2 and 3 in the axial and radial directions, respectively, are combined into another figure.

Typical Results for a Rotor

The Blade Circulation and Loading

The calculation of the nondimensional blade loading and circulation is performed before the calculation of the induced velocity in the wake. For better perspective, the plots of the blade circulation distribution, C (x), and the nondimensional thrust loading distribution, dC (x)/dx, are drawn against r/R instead of r/RA in Figure 5. The peaks of these curves are strong and occur very close to the tip of the blade. The peak value of C (x) is used in Eq. (II-9) to calculate the value of Q and is dependent on the distribution of the induced downwash. The peak in C (x) corresponds to a negative peak in the downwash distribution. The negative peak in the downwash distribution depends on the position with respect to the blade of the tip vortex from the preceding blade. The effect of the tip vortex from

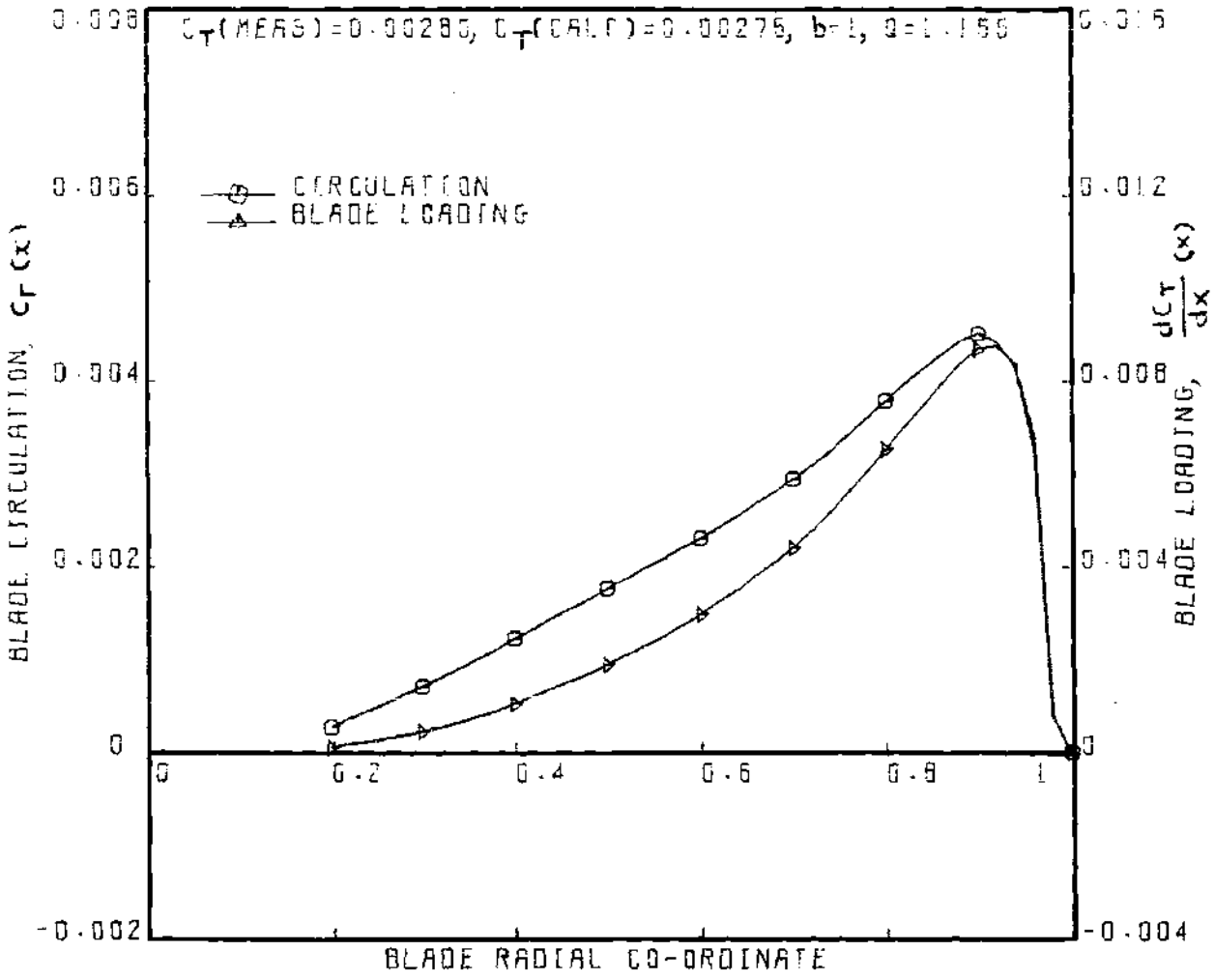

Figure 5. Blade Circulation and Loading for Condition No. 2.

the preceding blade is discussed in more detail in the case of a six-bladed rotor. The area under the $dC_T(x)/dx$ curve gives the thrust coefficient, C_T. The calculated value of C_T is in good agreement with the observed value for which the data is selected.

Empirically Derived Apparent Velocity

The empirically derived apparent velocity components are presented in their nondimensional form by a solid line in Figures 6a, 6b, and 6c. They are calculated using the first expression for u_a and w_a in the Eqs. (II-5), (II-8), and (II-11). These values depend upon the value of C_f which is constant for a given case. In Case 1, C_f is calculated in the ultimate wake. In Cases 2 and 3, it is calculated at the blade.

The empirically derived value of the radial component of the apparent velocity is proportional to $dx/d\psi$ which is calculated from Eq. (III-1). The $dx/d\psi$ is initially negative and increases to 0. The empirically derived radial component of the apparent velocity behaves similarly. Since the rate of contraction is greatest at $\psi=0$, the radial component is most negative there. In the ultimate wake where the tip vortex has constant diameter, it is zero, indicating no motion in the radial direction.

The empirically derived value of the axial apparent velocity is proportional to $dz/d\psi$. The axial coordinate of the tip vortex as described in Eqs. (III-2) is linear and

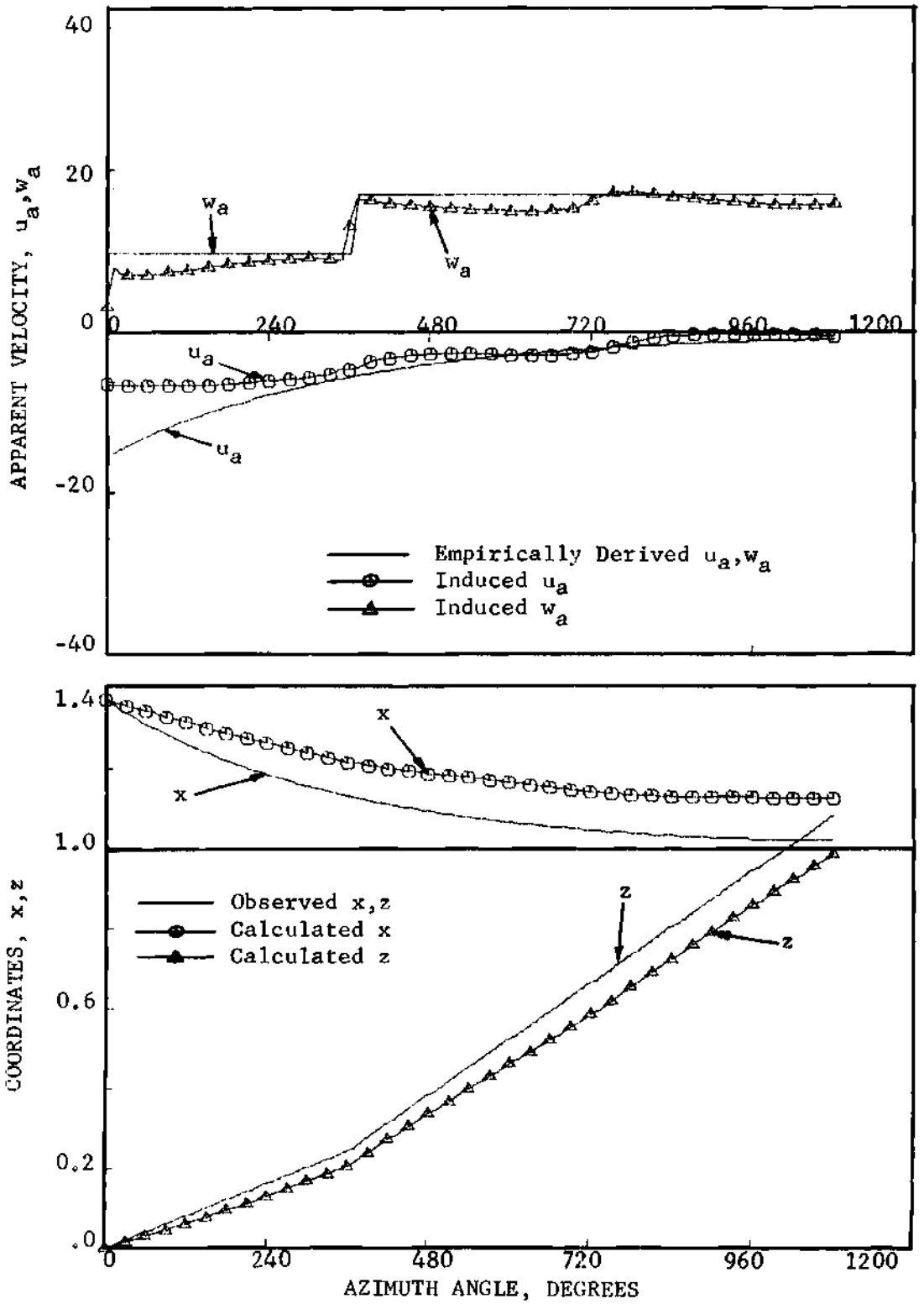

Figure 6a. Apparent Velocity and Geometry for Condition No. 2, Case 1, C_T=.00280, b=1.

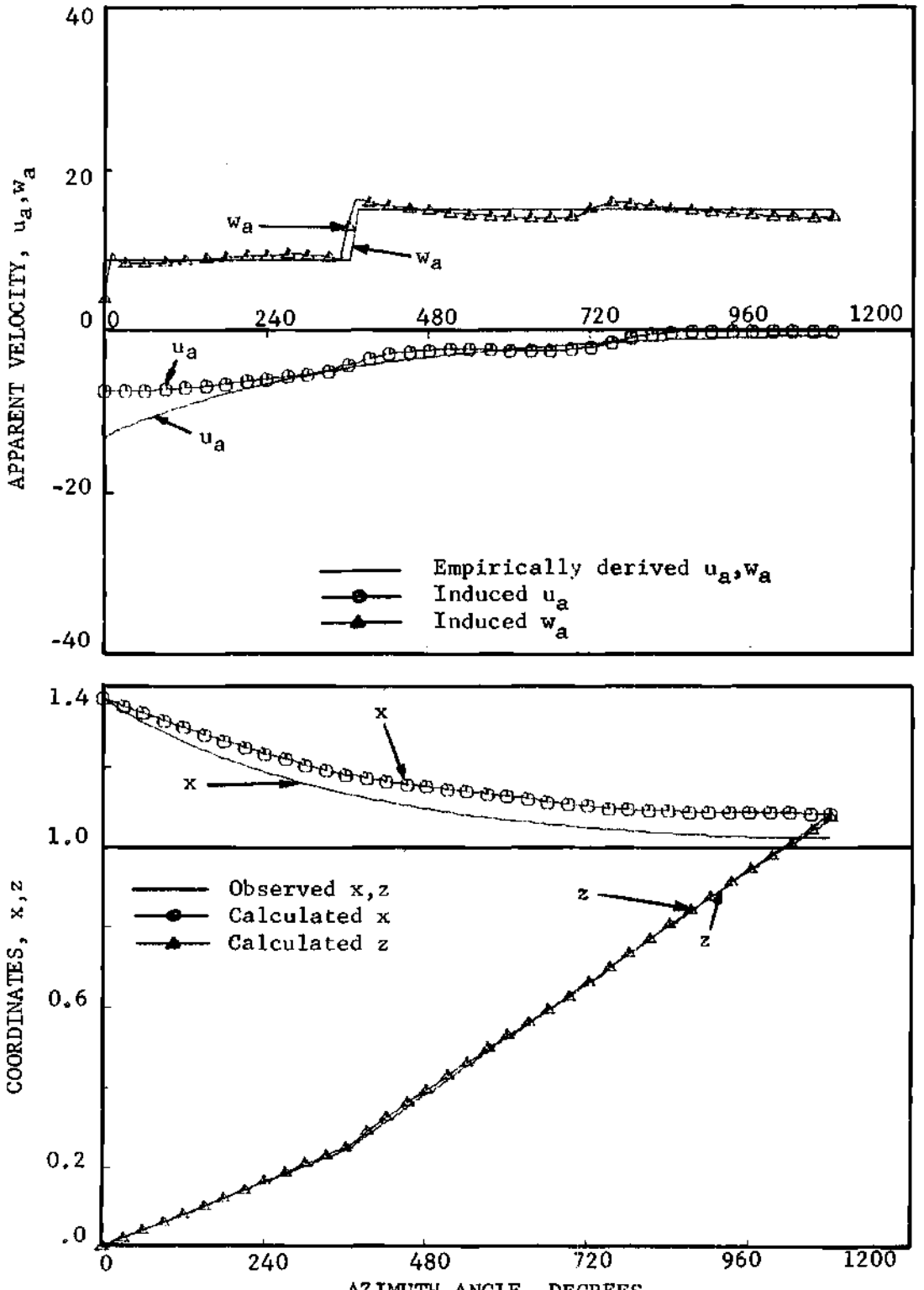

Figure 6b. Apparent Velocity and Geometry for Condition No. 2. Case 2, C_T=.00280, b=1.

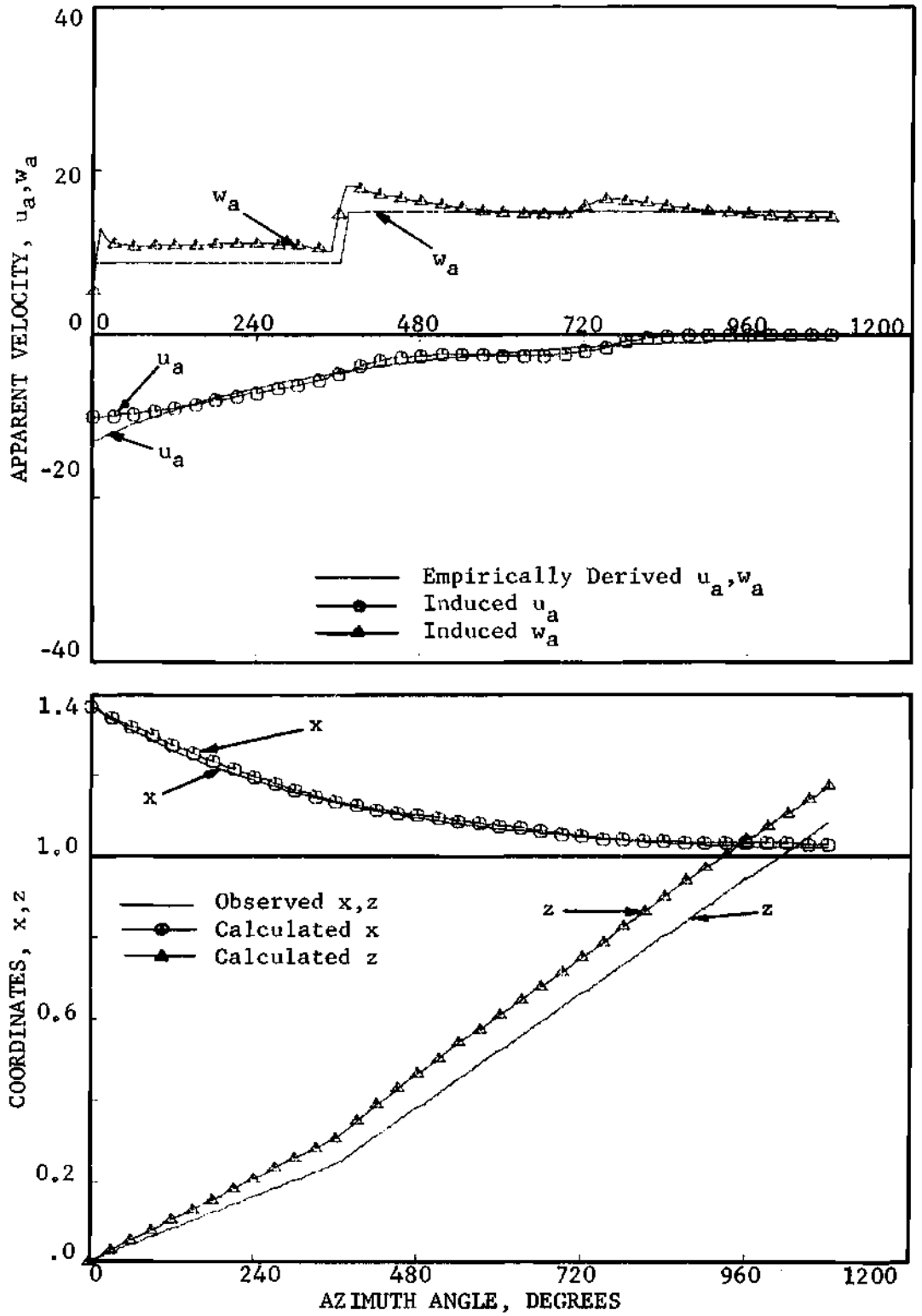

Figure 6c. Apparent Velocity and Geometry for Condition No. 2, Case 3, C_T=.00280, b=1.

has a break in the slope at $\psi=2\pi/b$. This break in the slope is primarily due to the tip vortex of the next following blade which is directly above the point at this azimuth angle. There is also an effect of the bound vortex of the following blade at locations immediately before and after $2\pi/b$. The empirically derived apparent axial velocity is constant up to and after $\psi=2\pi/b$. The empirical discontinuity in the slope and velocity that occurs at this point is proportional to (k_2-k_1).

Induced Apparent Velocity

The induced apparent velocity is obtained from the second expressions for u_a and w_a in Eqs. (III-5), (II-8), and (II-11). They are shown in the Figures 6a, 6b, and 6c by symbols joined with a line. For the proposed model and the corrections for the core effects to be acceptable, these induced components must be approximately the same as the empirically derived values of the corresponding components in the near wake. In the ultimate wake, the agreement is good as Eqs. (II-6) and (II-9) are satisfied exactly.

The apparent velocity components calculated in each of the three cases in this analysis are different since the correction applied in each case is different. However, the induced velocity components, u, v, and w, which are functions of the complex geometry of the vortex wake, are the same. The component v enters Eqs. (II-5), (II-8), and (II-11) in the form vC_T/x and it can be neglected with

respect to the other terms such as 1, Ω/x, and Ω/x^2. The axial component, w, is affected by the presence of the bound vortex especially at $\psi=0$ and $\psi=2\pi/b$. The effect of the bound vortex decreases rapidly as the blade moves away from this point. The effect of the bound vortex on the radial component, u, is small. The effect of the sheet is apparent only after certain azimuth locations since the sheet moves down very quickly and the points in the very near wake do not feel the effect of the sheet strongly.

In Case 1, Figure 6a, the induced apparent velocity components are appreciably smaller than the empirically derived values. This appears to be due to the lack of accounting for the effects of the core as noted earlier. Both the racial and axial components are not large enough and this leads to the discrepancy in the calculated geometry, namely, a smaller than observed inward and axially downward motion.

In Case 2, Figure 6b, the correction brings the calculated apparent velocities closer to the empirically derived values. The effect of the correction is different for the two components in the axial and radial directions but the axial component matches very closely with the empirically derived value. The induced radial component, while in closer agreement, is still not satisfactory.

In Case 3, Figure 6c, the correction brings the induced radial component very close to the empirically

derived value and the axial component is overcorrected.

Calculated Geometry

The induced apparent velocities for the observed geometry of the tip vortex are integrated to calculate the next geometry of the tip vortex using Eqs. (III-12). The integrals are calculated by the trapezoidal rule. The displacement curves are smoother than the velocity curves as an effect of the integration. The calculated coordinates are shown in the figures by symbols connected by a line. These are compared with the observed geometry whose data points have been faired and approximated by Eqs. (III-1) and (III-2).

In Case 1 (Figure 6a) the calculated coordinates fall appreciably short of those observed. The discrepancies in the coordinates are cumulative and the coordinates at the azimuth locations farther down the wake are farther from the corresponcing observed coordinates. The z and x coordinates obtained for Cases 2 and 3 (Figures 6b and 6c respectively) match closely with the observed coordinates.

Results for Other Rotors

Single-Bladed Rotor

The vortex system for the single-bladed rotor is the simplest since there is only one vortex element of each kind. The observed geometry was obtained from Ref. 8. Condition No. 2 has already been considered and corresponds

to a thrust coefficient in the middle of the range for which the data were available. Condition Nos. 1 and 3 represent thrust coefficients that are lower and higher than this. The results for Condition Nos. 1 and 3 are presented in Figures 7 and 8 respectively. The discrepancies in the calculated velocity and the geometry are quite apparent in Figures 7a and 8a. Results for Case 2 with axial component and Case 3 with radial component are presented in Figures 7b and 8b and show good agreement between the induced and empirically derived values. The resulting geometry agrees well with that observed.

Two-Bladed Rotor

As for the single-bladed rotor, a two-bladed rotor was considered for three values of thrust coefficient. The geometric data were obtained from Ref. 4. The sheet geometry calculations take an appreciably long time, hence, only one iteration of the sheet geometry was performed. The results for the three different thrust coefficients are presented in Figures 9 to 11. Case 1 is shown in Figures 9a, 10a and 11a and the results with the correction are shown in Figures 9b, 10b and 11b. The corrected apparent velocities and geometries match closely with the empirically derived values for all three thrust conditions.

Six-Bladed Rotor

After the success of the method with the one- and two-bladed rotors, calculations for a six-bladed rotor were

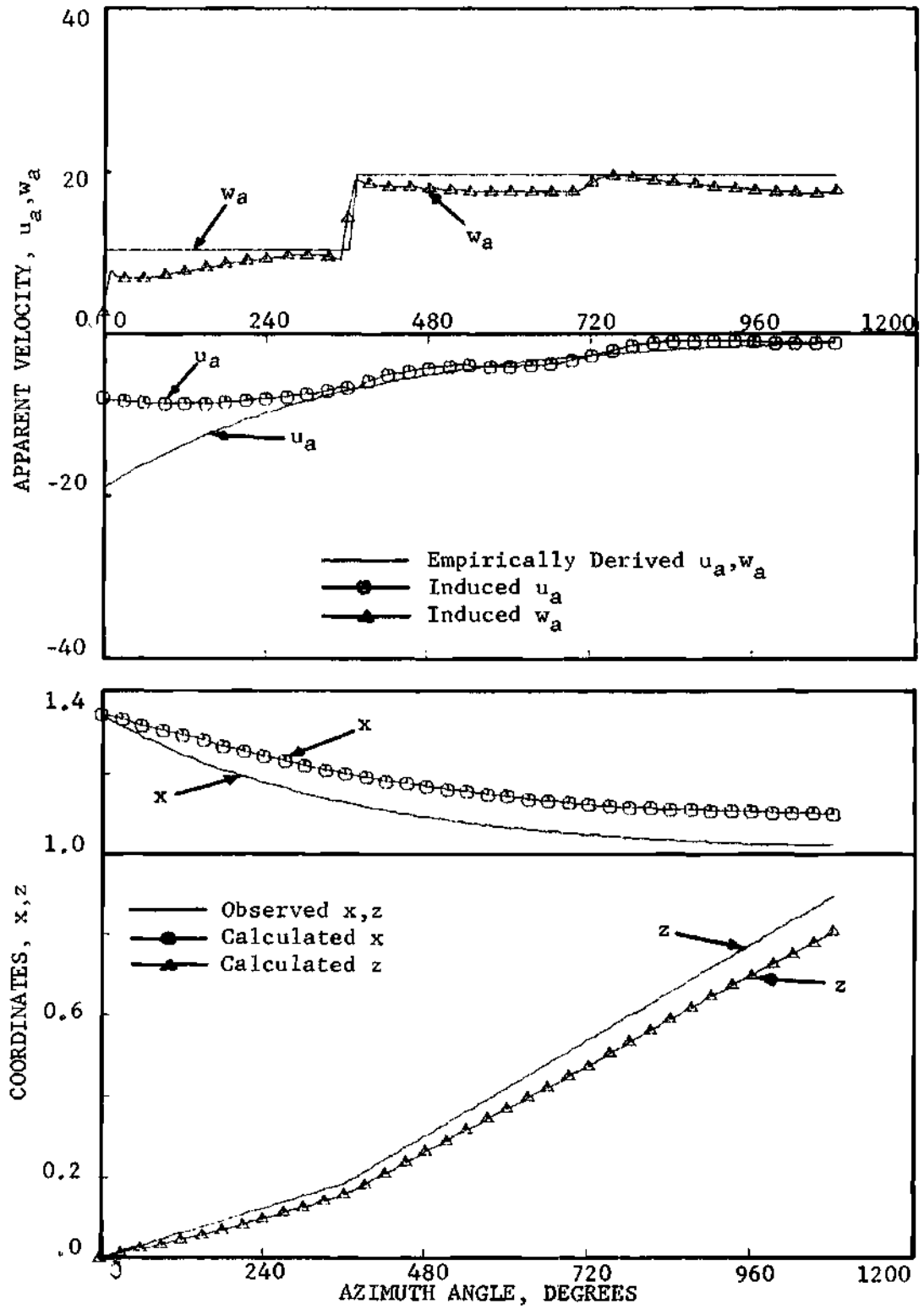

Figure 7a. Apparent Velocity and Geometry for Condition No. 1, Case 1, C_T=.00195, b=1.

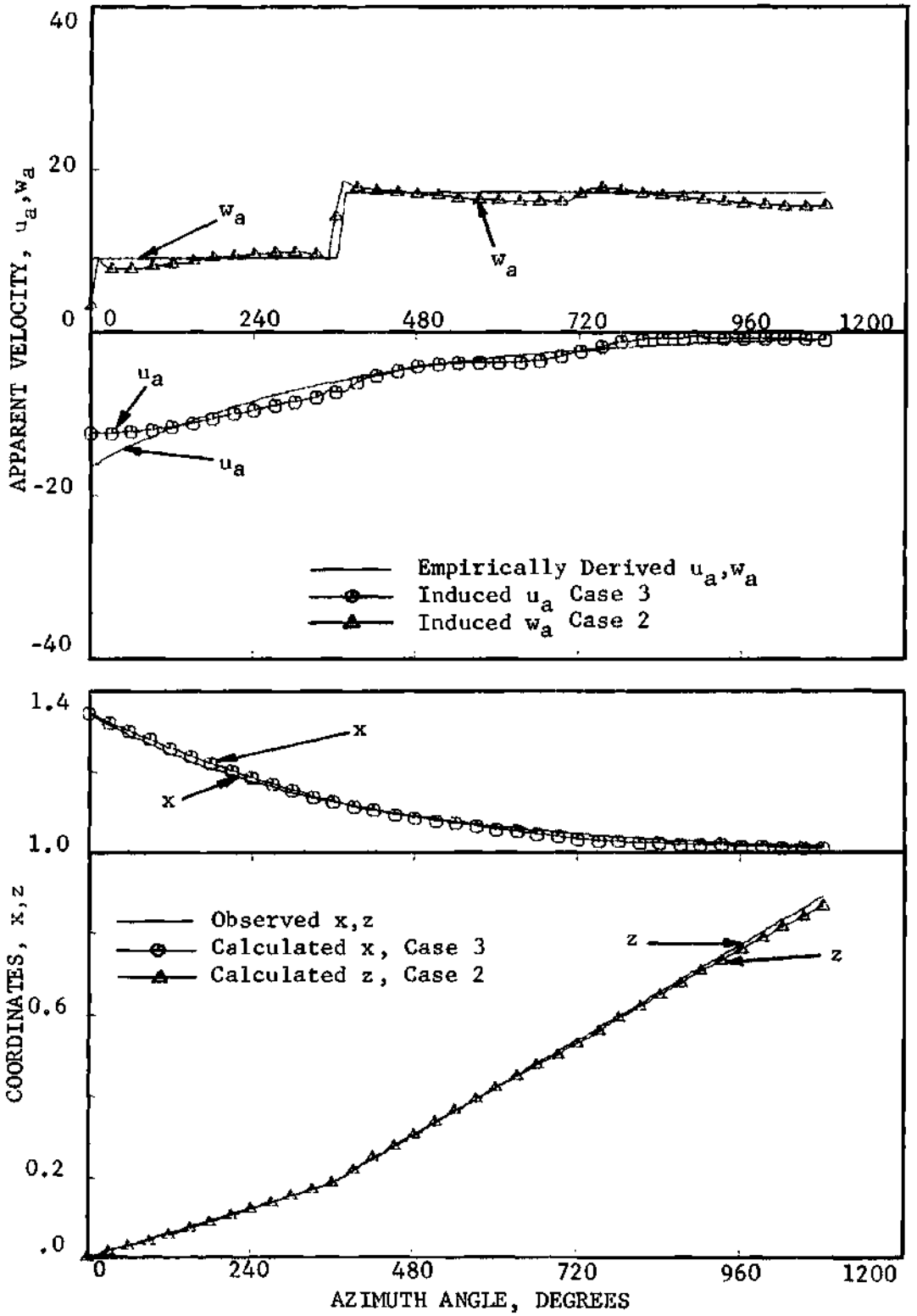

Figure 7b. Apparent Velocity and Geometry for Condition No. 1, Cases 2 and 3, C_T=.00195, b=1.

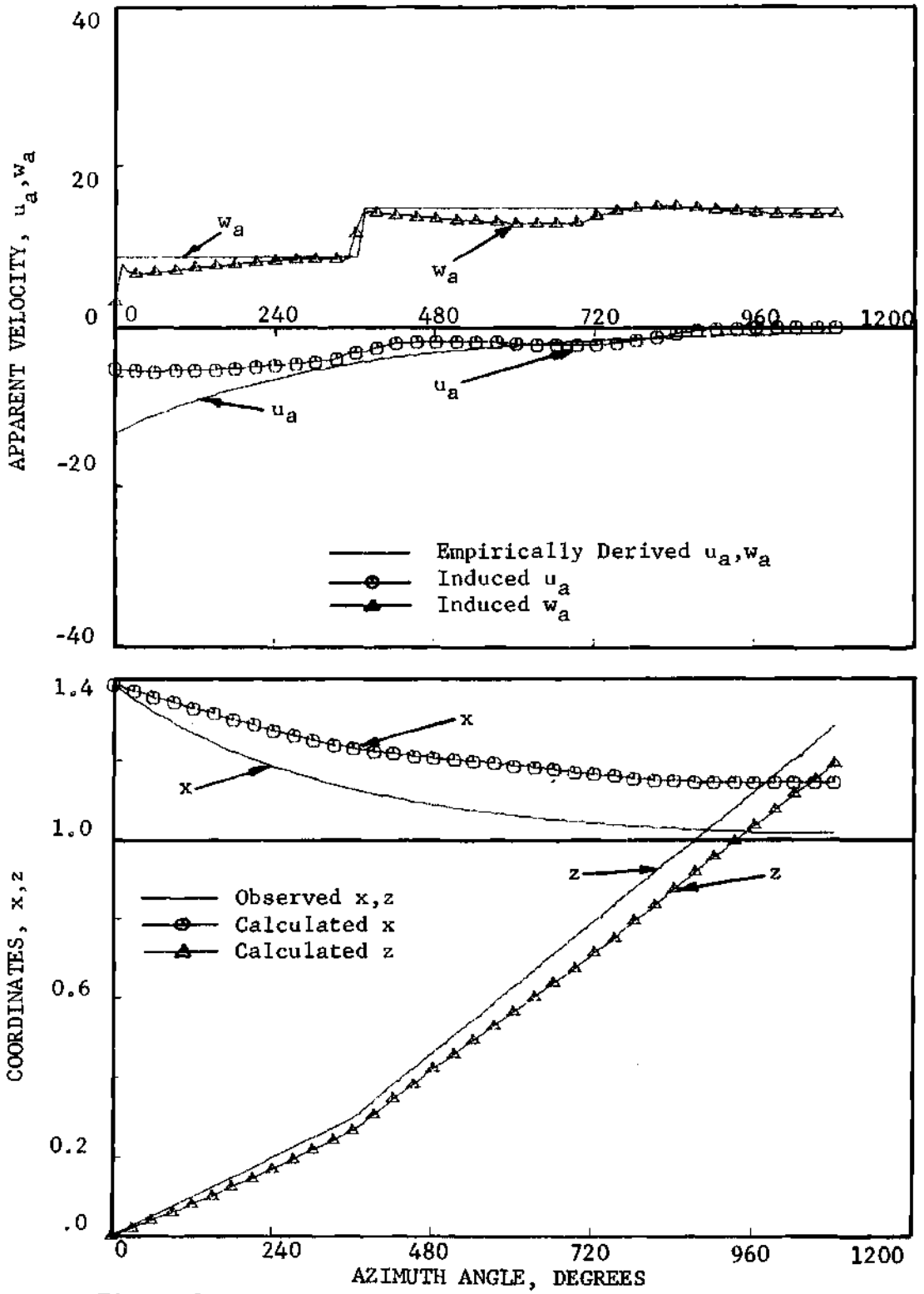

Figure 8a. Apparent Velocity and Geometry for Condition No. 3, Case I, C_T=.00370, b=1.

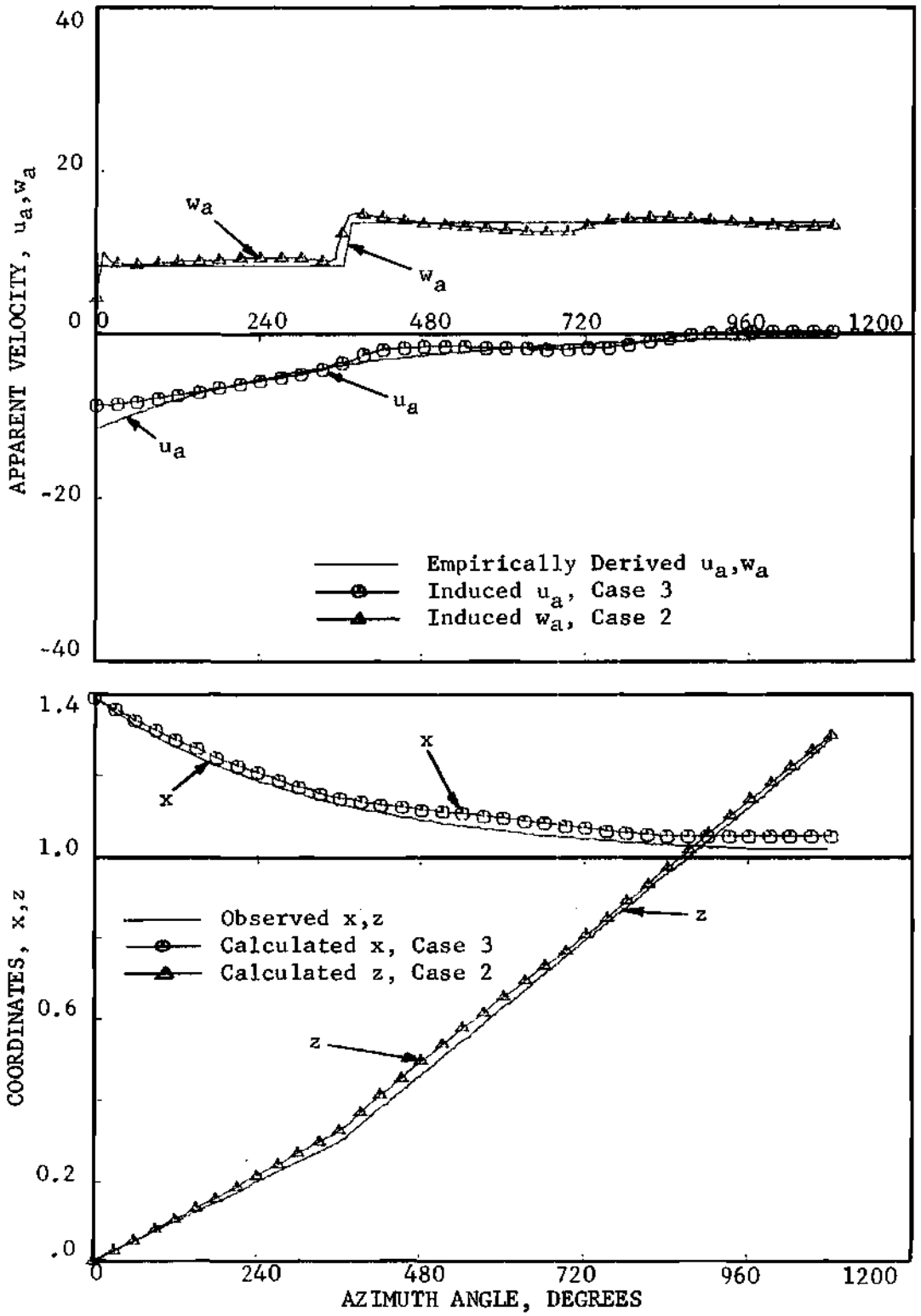

Figure 8b. Apparent Velocity and Geometry for Condition No. 3, Cases 2 and 3, C_T=.00370, b=1.

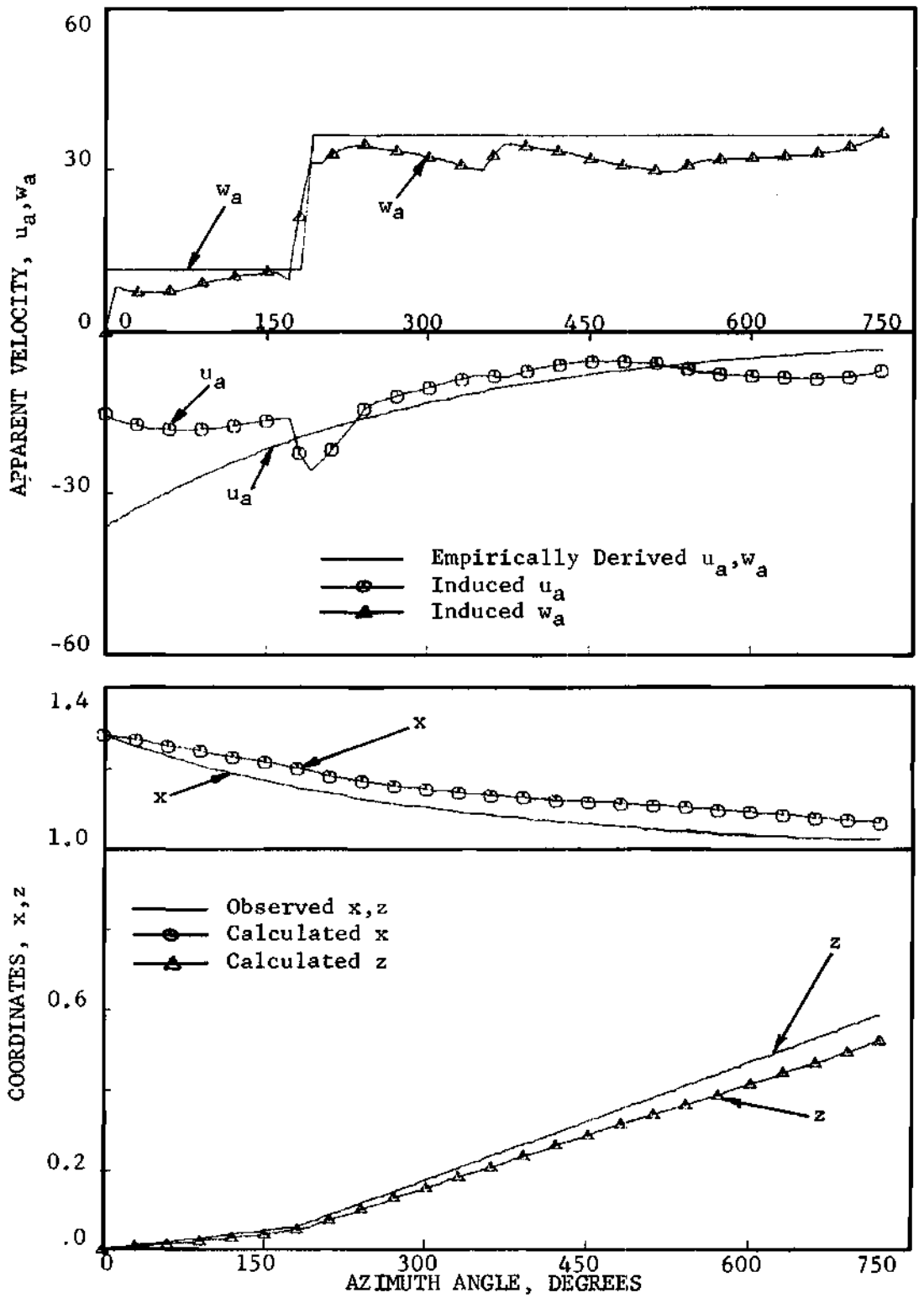

Figure 9a. Apparent Velocity and Geometry for Condition No. 4, Case 1, C_T=.00193, b=2.

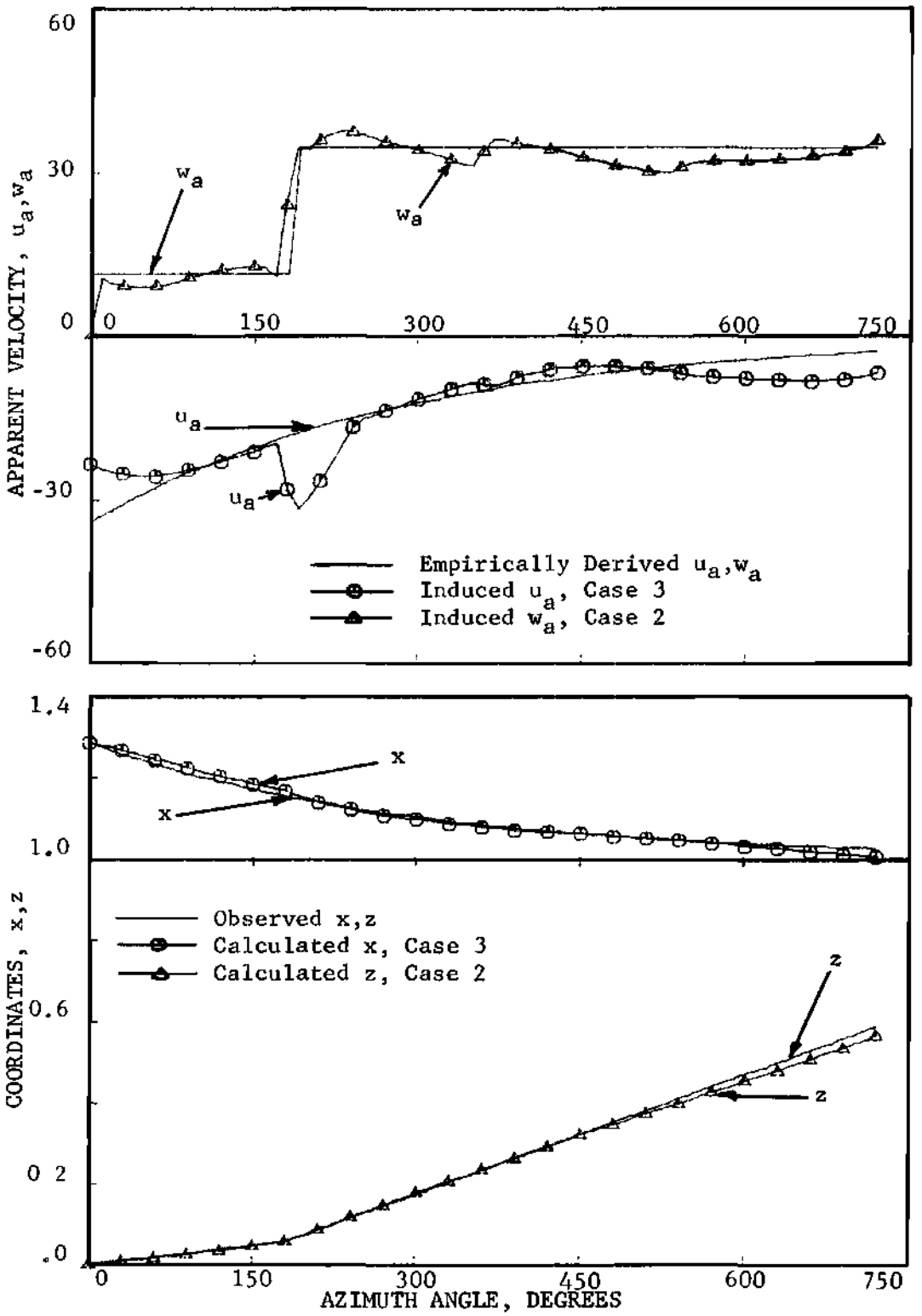

Figure 9b. Apparent Velocity and Geometry for Condition No. 4, Cases 2 and 3, C_T=.00193, b=2.

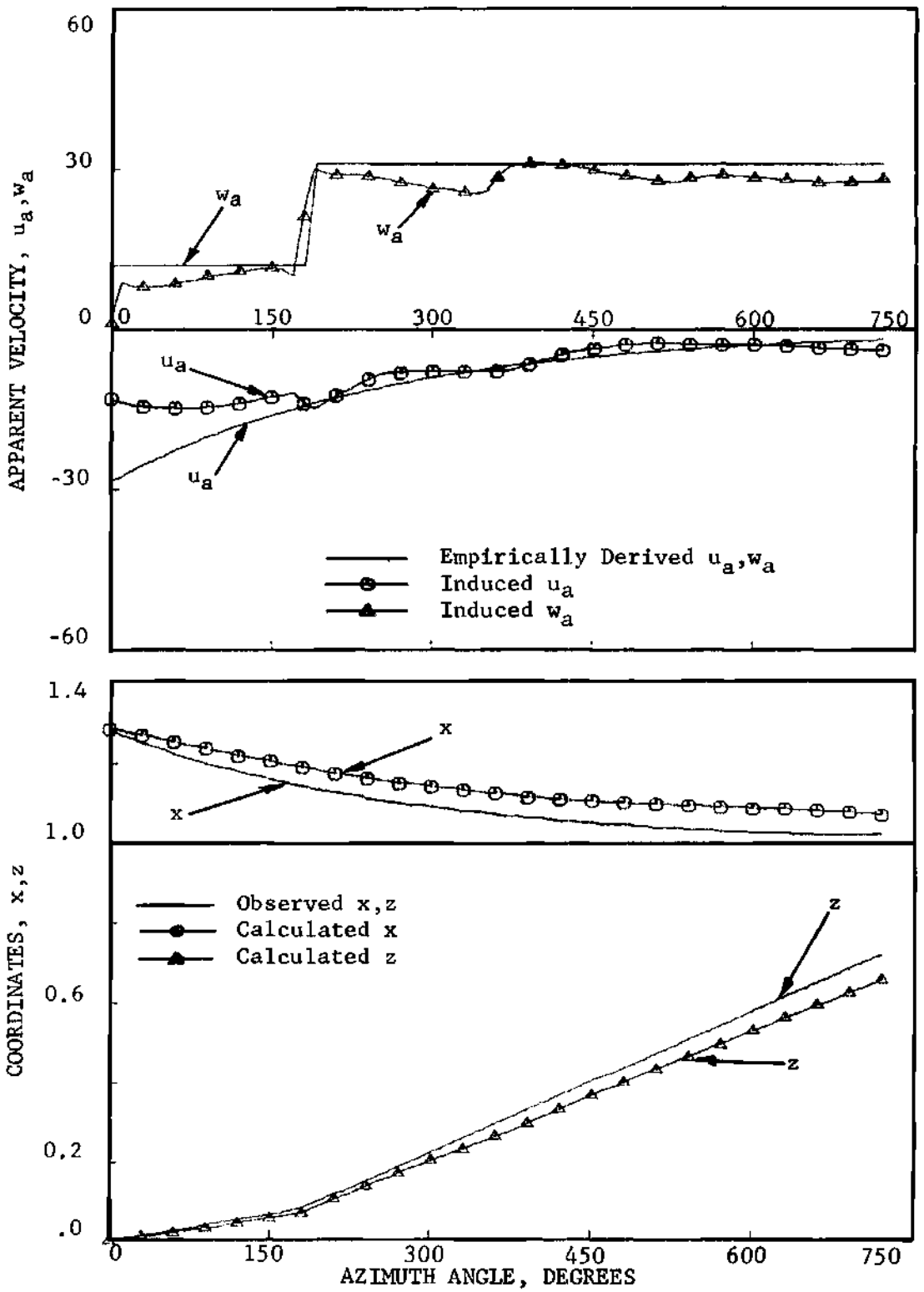

Figure 10a. Apparent Velocity and Geometry for Condition No. 5, Case 1, C_T=.00283, b=2.

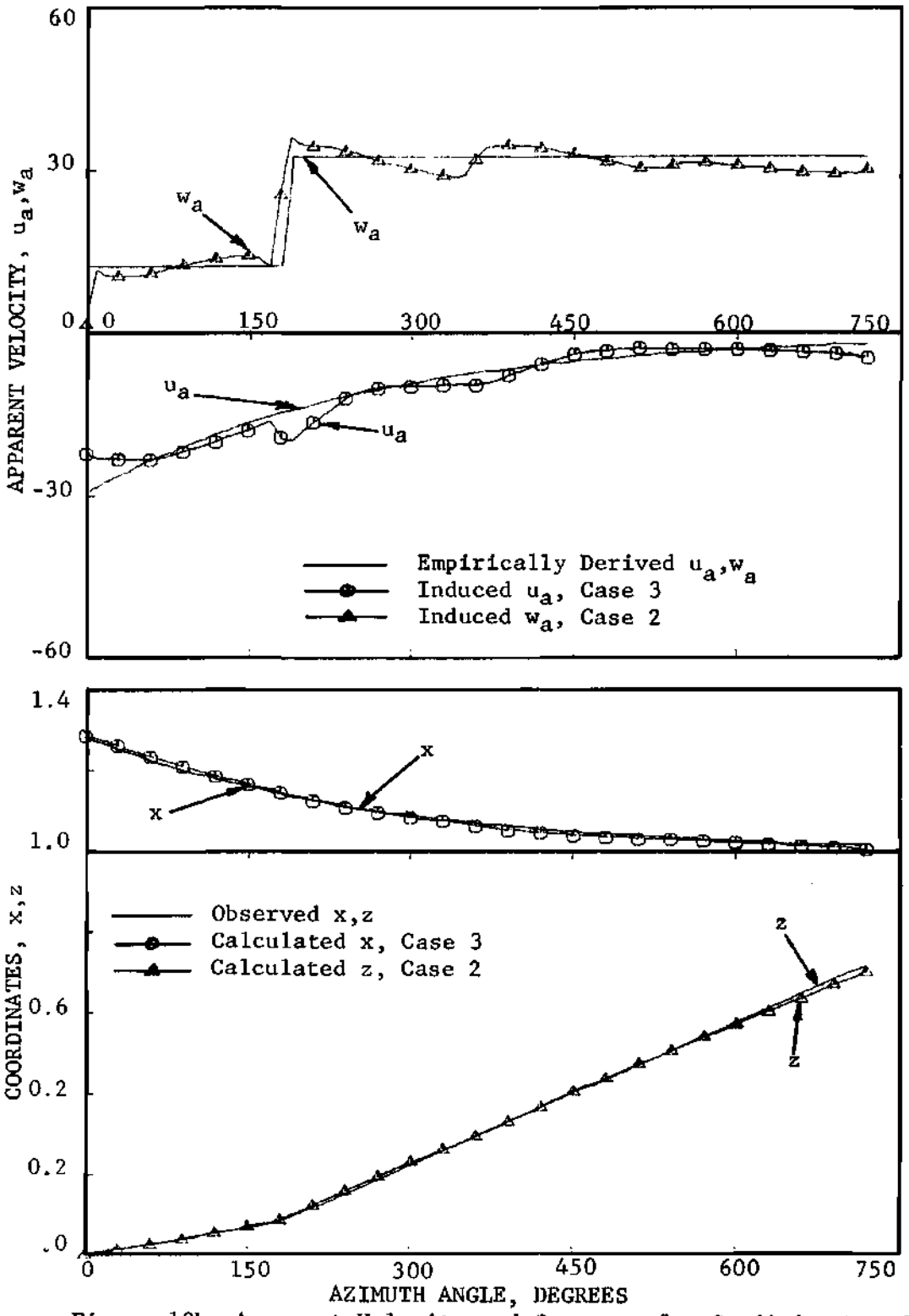

Figure 10b. Apparent Velocity and Geometry for Condition No. 5, Cases 2 and 3, C_T=.00283, b=2.

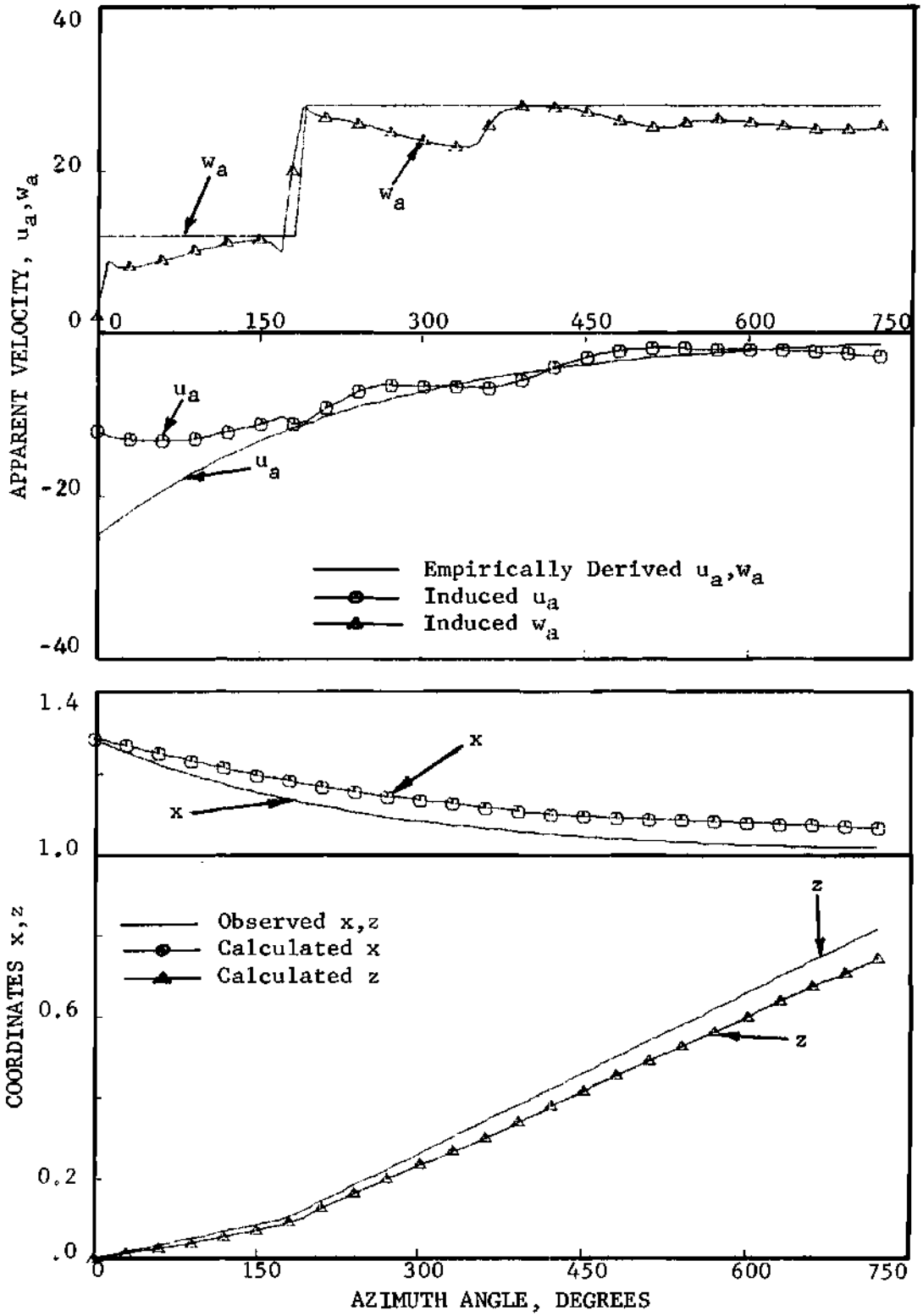

Figure 11a. Apparent Velocity and Geometry for Condition No. 6, Case 1, C_T=.00350, b=2.

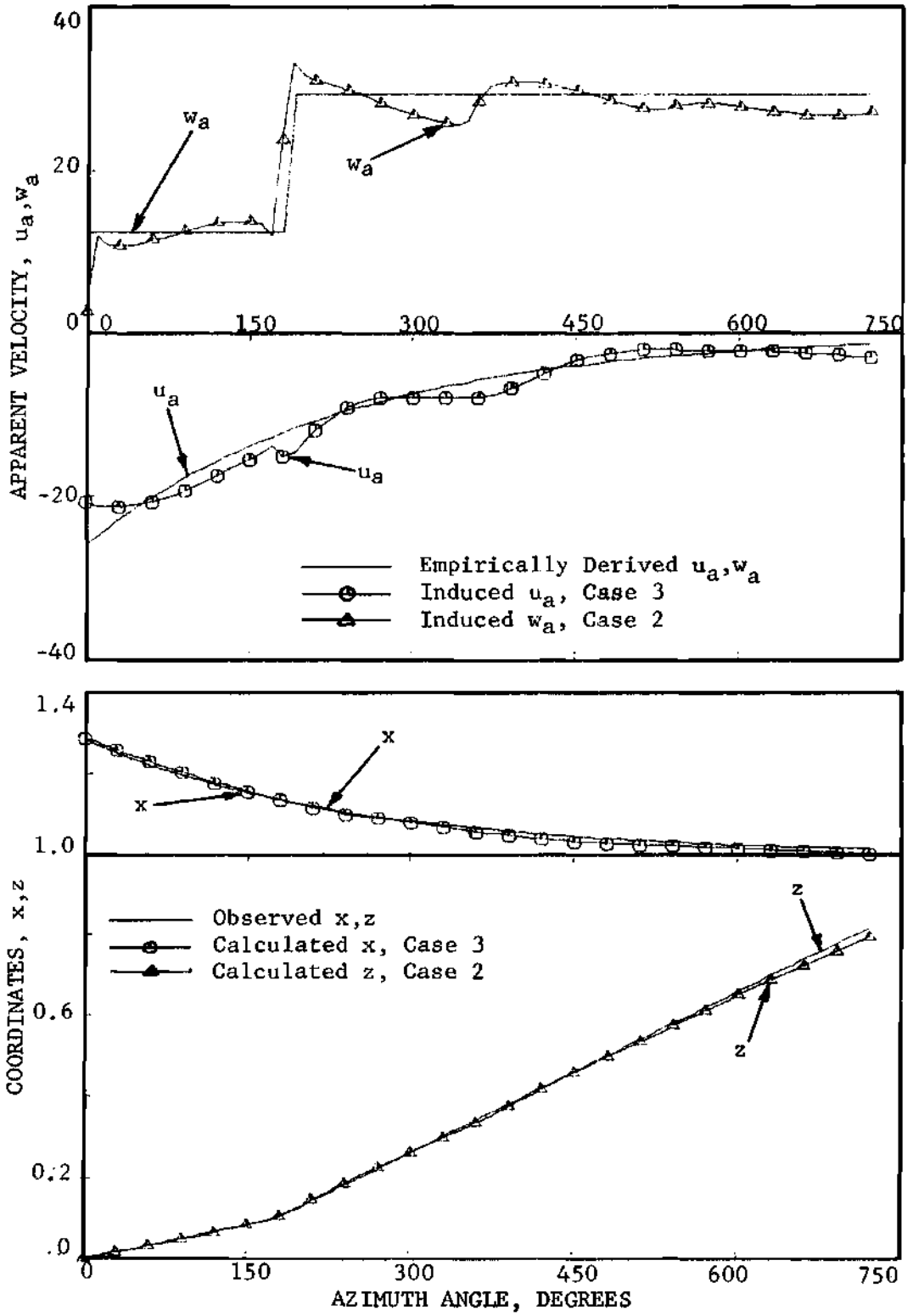

Figure 11b. Apparent Velocity and Geometry for Condition No. 6, Cases 2 and 3, C_T=.00350, b=2.

undertaken. The data for the geometry of the six-bladed rotor were obtained from Ref. 4. The induced downwash distribution at the blade due to the tip vortex elements showed a strong negative peak near the tip region and the resulting circulation distribution showed a very strong peak. The negative peak in the induced downwash was due to the close proximity of the tip vortex from the preceding blade. In fact, the six-bladed rotor measurements indicated that the tip vortex was intercepted by the next following blade. The lifting line theory is not valid in such a circumstance and the procedure for determining $C_{\Gamma}(x)_{max}$ and Q did not give reasonable results. Further efforts to work on the six-bladed rotor were abandoned and calculations for three- and four-bladed rotors were undertaken.

Three- and Four-Bladed Rotors

The geometric data for the three- and four- bladed rotors were obtained from Ref. 11. Two thrust conditions for the three-bladed rotor, Condition Nos. 7 and 8, and one thrust condition for the four-bladed rotor, Condition No. 9, were considered. The sheet geometry calculations are carried through two iterations for each of Condition Nos. 7 through 9. Figures 12 through 14 show the results obtained for Condition Nos. 7 through 9. The same trends as observed in the one- and two-bladed rotor calculations are observed here.

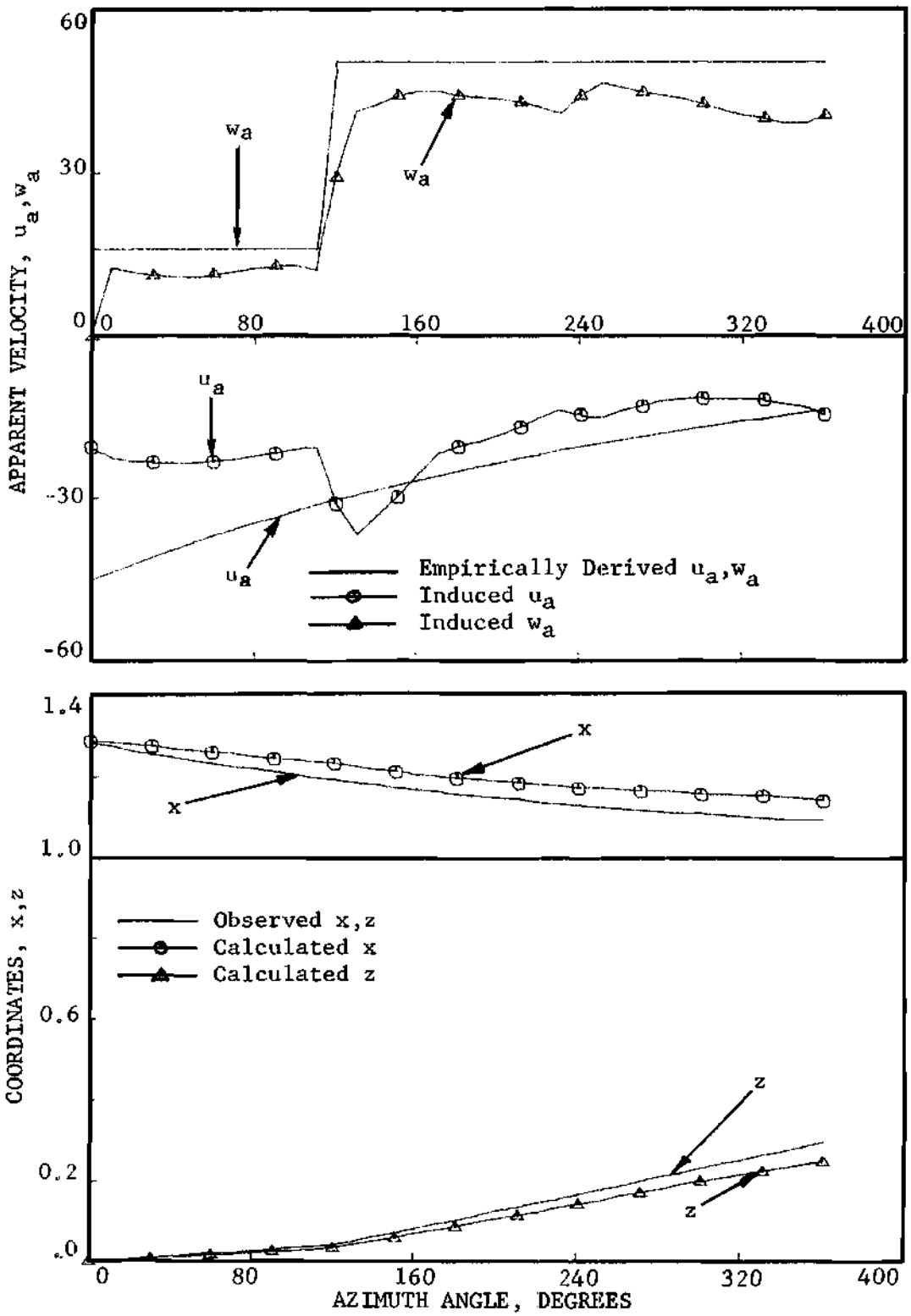

Figure 12a. Apparent Velocity and Geometry for Condition No. 7, Case 1, C_T=.00220, b=3.

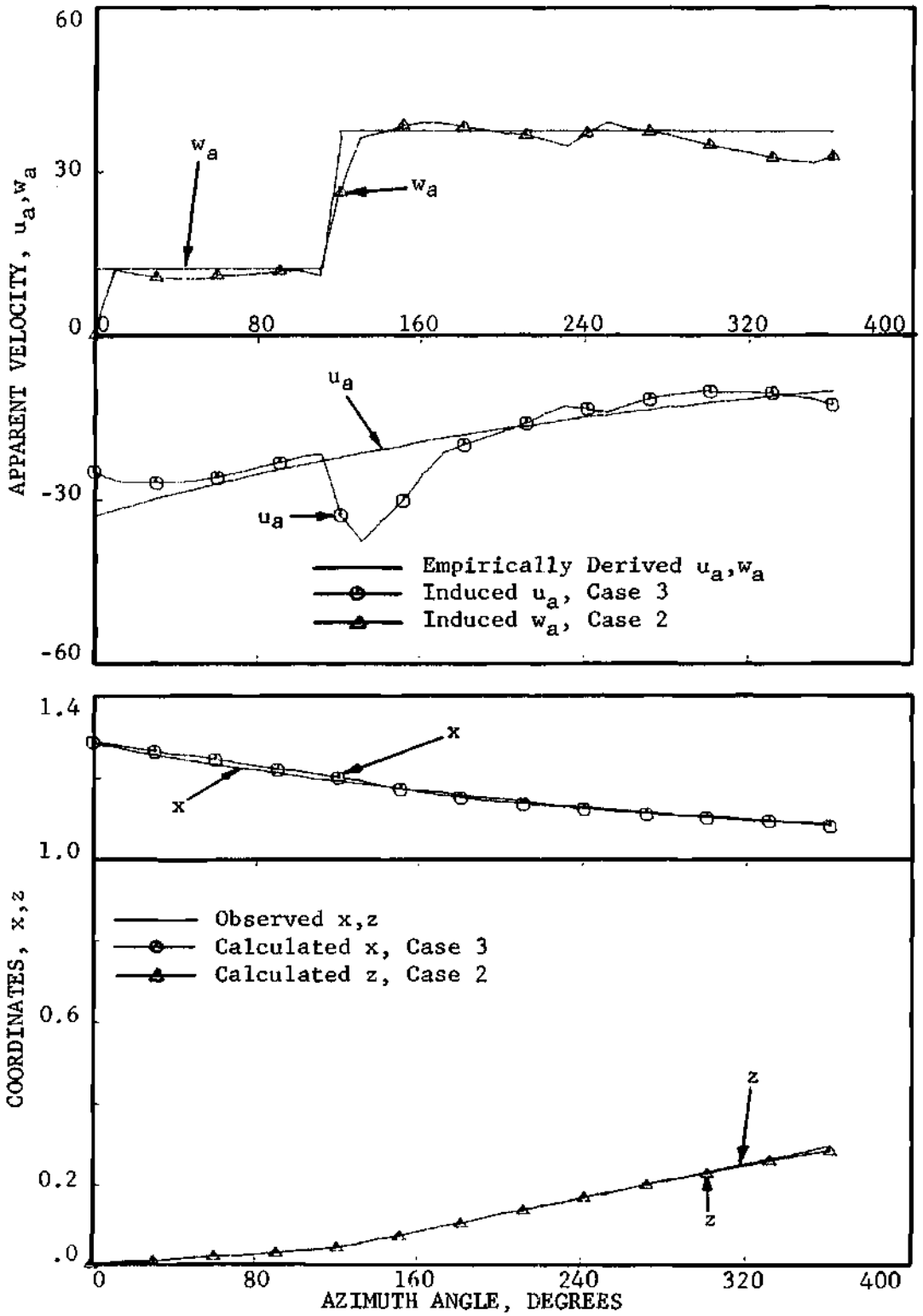

Figure 12b. Apparent Velocity and Geometry for Condition No. 7, Cases 2 and 3, C_T=.00220, b=3.

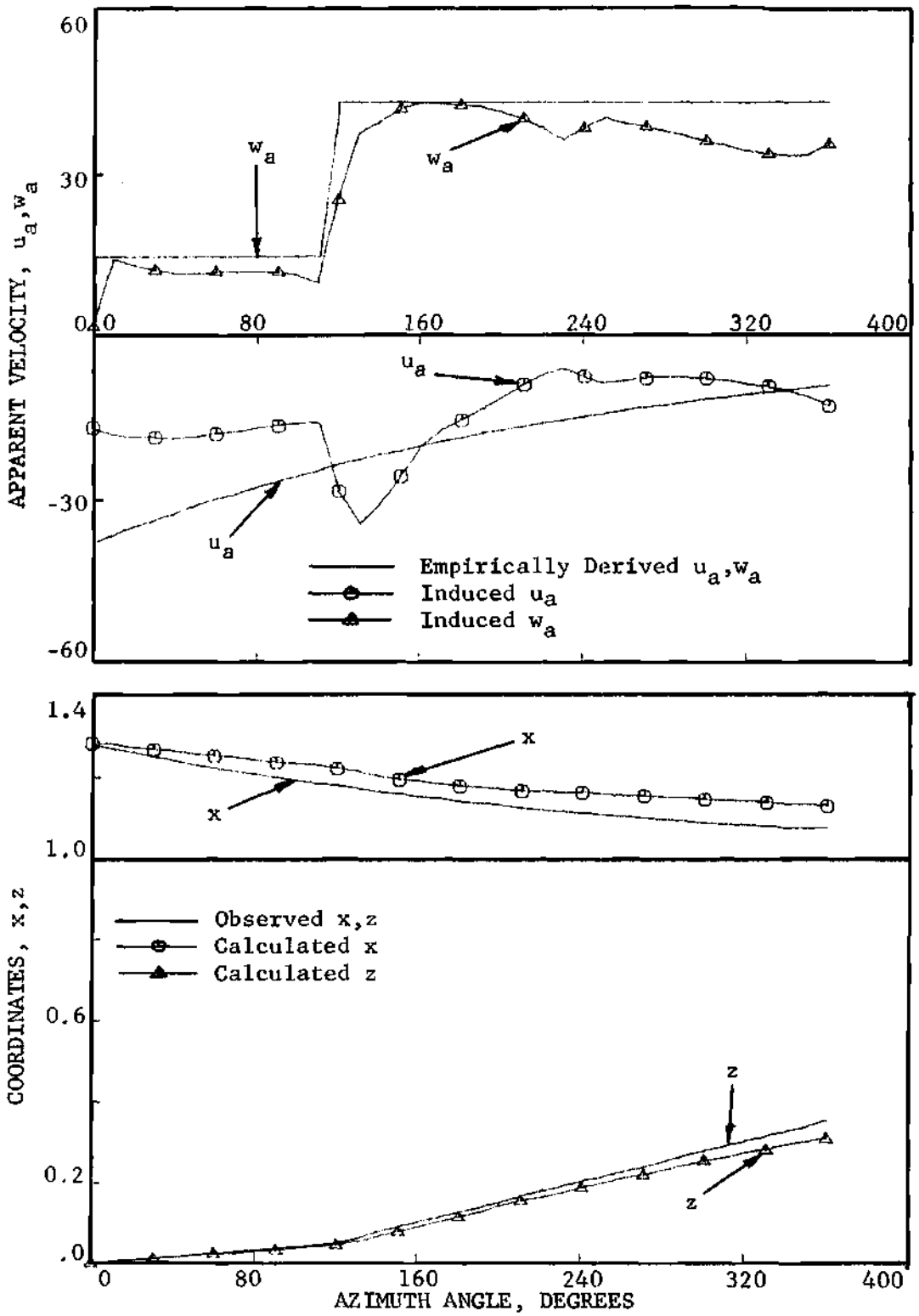

Figure 13a. Apparent Velocity and Geometry for Condition No. 8, Case 1, C_T=.00320, b=3.

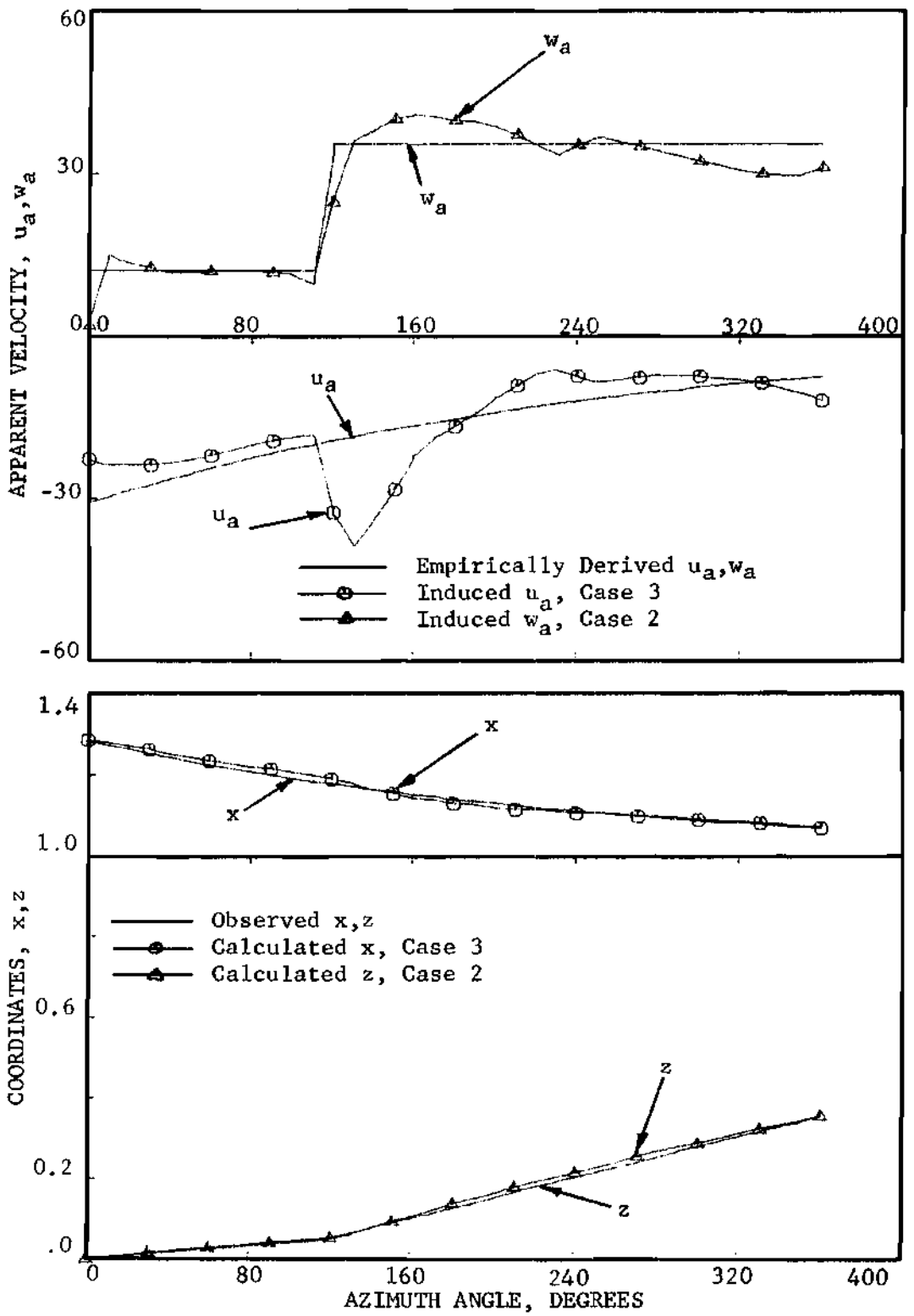

Figure 13b. Apparent Velocity and Geometry for Condition No. 8, Cases 2 and 3, C_T=.00320, b=3.

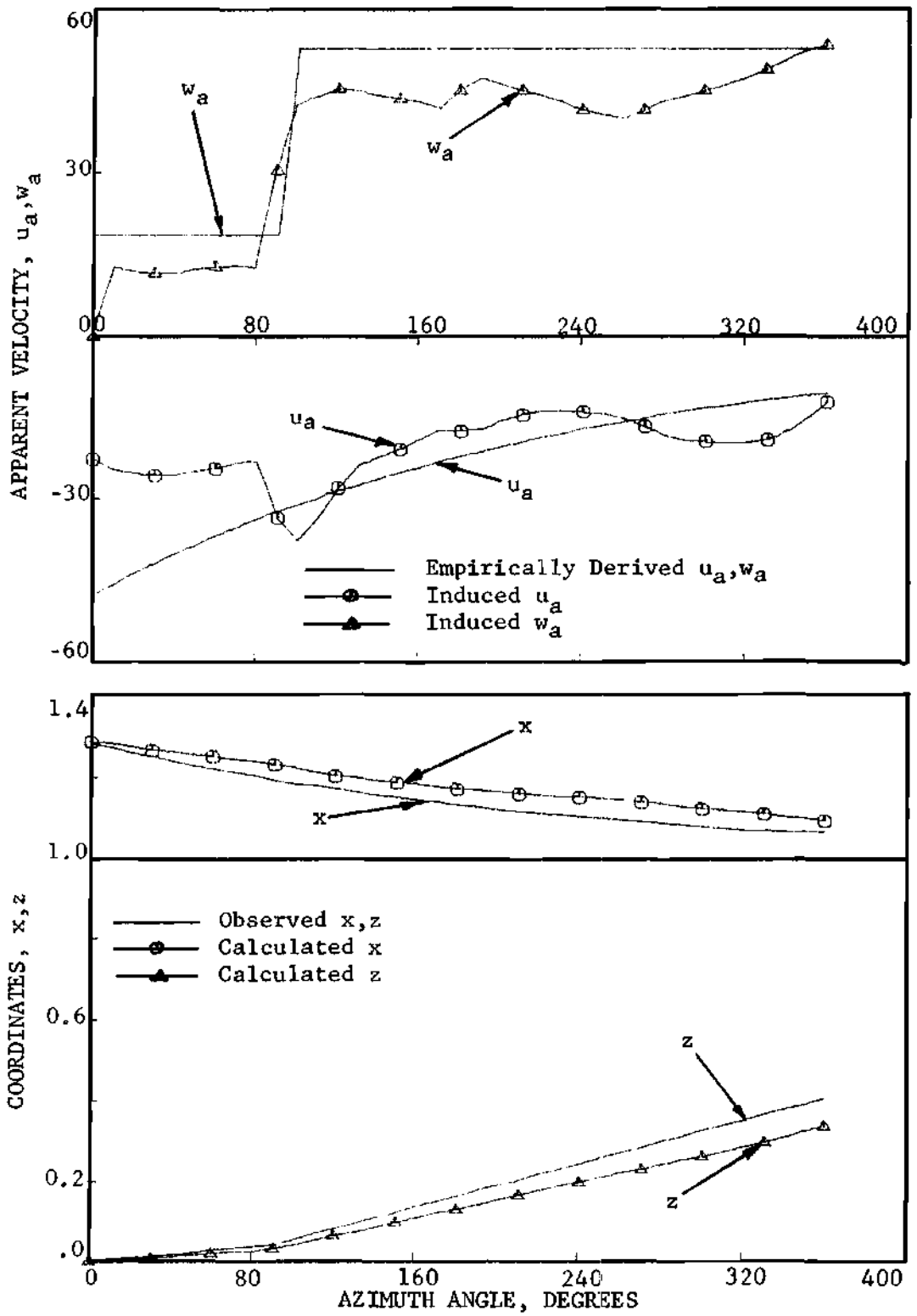

Figure 14a. Apparent Velocity and Geometry for Condition No. 9, Case 1, C_T=.00371, b=4.

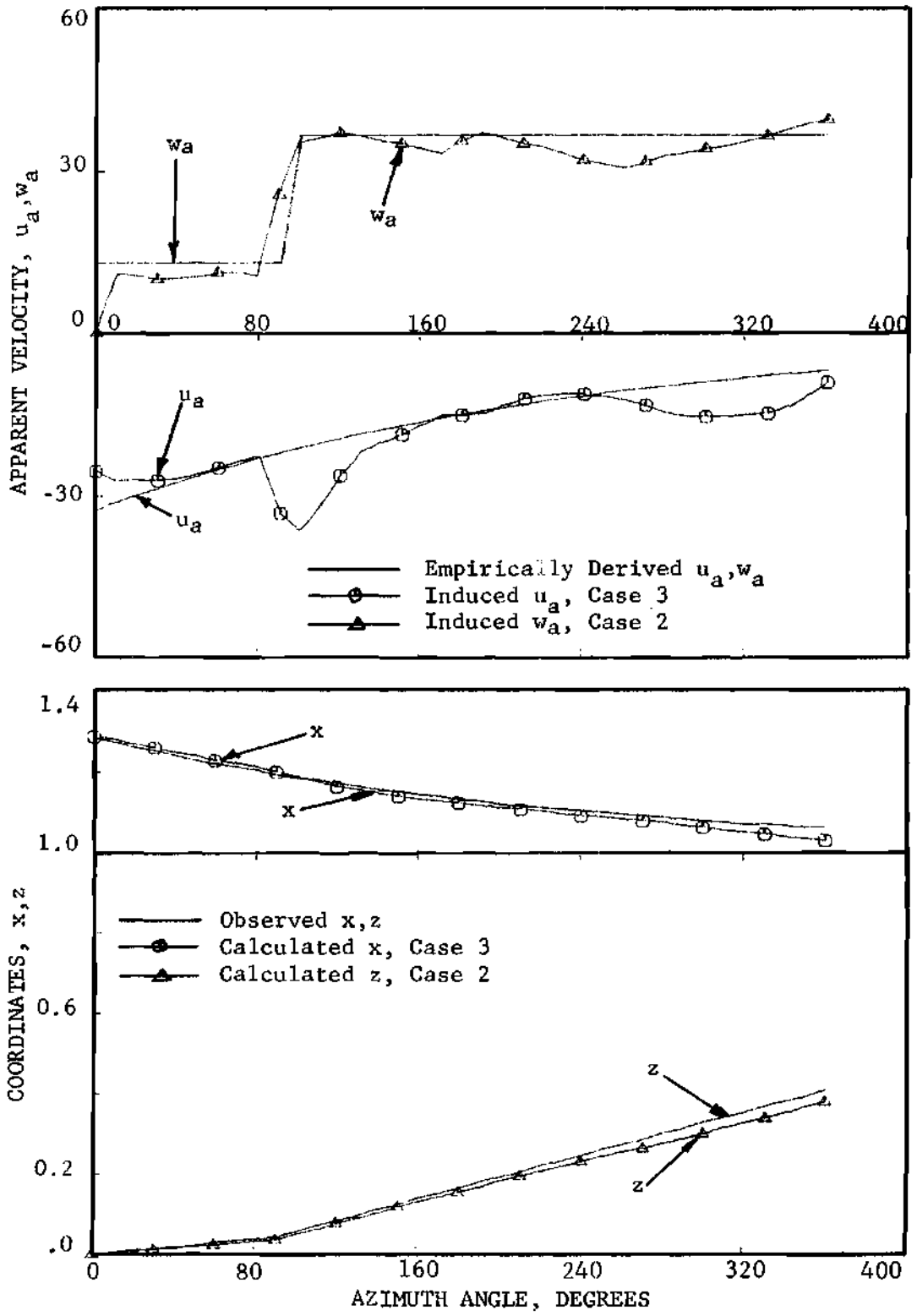

Figure 14b. Apparent Velocity and Geometry for Condition No. 9, Cases 2 and 3, C_T=.00371, b=4.

Additional Comments

The Effect of the Sheet Filaments

The apparent velocity components shown in these figures show negative peaks at certain azimuth locations, e.g., see Figure 9a near ψ=190. These peaks are the result of the presence of the sheet filaments which have concentrated vorticity as opposed to the continuous vorticity of the sheet they approximate. If the number of filaments is increased, then the intensity of the peaks reduces. For one- and two-bladed rotor wakes, five filaments were found sufficient. The peaks in these wakes are small and do not affect the geometry calculations appreciably. The three- and four-bladed rotors, however, showed large peaks that did affect the geometry calculation. Hence, ten filaments were used in Condition Nos. 7 through 9 to get satisfactory results.

Value of C

The values of C given in the table show certain trends. For a given number of blades, the value of C decreases as C_T increases. However, there is no trend shown with the change in the number of blades. The one thing that is noticeable, however, is that C is larger for three- and four-bladed rotors than for one- and two-blaced rotors. This is primarily due to the fact that the tip vortex from the preceding blade for a higher number of blades passes much closer to the rotor thus altering the downwash

distribution in the tip region considerably.

Computer Time

The computer time required for a typical single-bladed Condition is about 10 minutes on the CDC 6400 computer. The computer time for a higher number of blades is approximately proportional to the number of blades. About 70 to 80 per cent of this time is used in the sheet geometry calculations. The tip vortex integrations were carried out for 25 turns of the tip vortex helix in the wake. Some reduction in the computer time could have been achieved by approximating the integrals in Eqs. (III-8) when the integration is performed far away from the point at which the velocity is calculated.

CHAPTER V

CONCLUSIONS AND RECOMMENDATIONS

Conclusions

1. The theoretical apparent induced velocities calculated using the method of Ref. 5 are less than the empirically derived values both in the radial and axial directions. In so far as the external effects of the vortices are concerned, the treatment in this analyses is complete. The core effect is modelled only for the axial component. The discrepancies in the apparent velocities may be considered as resulting from the inadequate treatment of the core effects in the other two directions.
2. A steady vortex filament referenced in the blade coordinate system fixed to the blade has to be a streamline in the flow field and hence the induced velocity must satisfy certain relations, Eqs. (II-2), called consistency requirements. The induced velocities calculated for an observed geometry do not satisfy these relation when treated as in Ref. 5 (Case 1 of this analysis).
3. The consistency requirements can be satisfied to a better degree by modifying the v_s in the calculation of the

apparent components. A separate correction is applicable to each component of the apparent velocities, Case 2 for the axial, and Case 3 for radial.

4. An inconsistency is introduced in the analysis when the corrections in Cases 2 and 3 are used simultaneously, namely, that the azimuth components of the actual velocity are different. The inconsistency in the analysis is resolved when the insignificant term, vC/x, is neglected, and the resulting analysis yields two corrections, one to the azimuth component, and the other to the radial component.
5. The method is applicable for rotors having one to four blades and operating at different thrust levels.
6. The lifting line approximation for the blade becomes poorer as the number of blades increases.
7. A greater number of filaments is required to adequately approximate the inner vortex sheet as the number of blades increases.

Recommendations

1. The corrections suggested in this analysis to the velocity in the wake should be incorporated into a theoeretical analysis which calculates the tip vortex geometry.
2. Analysis of the tip vortex formation mechanism that will give irsight into the structure of the vortex core in the

near wake where its effect is most dominant should be performed.

3. Numerical experiments should be performed with various models of the tip vortex core in order to find a more analytical basis to these corrections.
4. An experimental program should be undertaken to investigate the axial motion inside of the core of the tip vortex.
5. A finite difference solution of the Navier-Stokes Equations should be obtained to establish the vortex core structure and the adjacent flow field.

BIBLIOGRAPHY

1. A. Gessow, and G.C. Meyers Jr. "Aerodynamics of the Helicopter." Ungar Publishing Co. N.Y., 1967.

2. M.C. Cheney Jr. and A.J. Landgrebe. "Rotor Wakes, Key to Performance Prediction." AGARD Confrence Preprint 111 on Aerodynamics of Rotary Wings. Marseilles, France. Sept. 72.

3. D.S. Jeney, J.R. Olson and A.J. Landgrebe. "A Reassessment of Rotor Hovering Performance Prediction Methods." Journal of AHS, V 13, No. 2. April 1968.

4. A. J. Landgrebe. "An Analytical and Experimental Investigation of Helicopter Rotor Hover Performance and Wake Geometry Characteristics." USAAMRDL TR 71-24. May 71.

5. R.B. Gray and G.W. Brown. "A Vortex Wake Analysis of a Single-Bladed Hovering Rotor and a Comparison with Experimental Data." AGRAD Conference Pre-Print 111 on Aerodynamics of Rotary Wings. Marseilles, France. Sept. 71.

6. S. Goldstein. "On the Vortex Theory of Screw Propellers." Royal Society of London Proceedings, V 123. 1929.

7. C.N. Lock. "Application of Goldstein's Airscrew Theory to Design." British ARC R&M 1377. 1930.

8. R.B. Gray. "On Motion of Vortex Shed from a Single-Bladed Hovering Model Helicopter Rotor and Its Application to the Calculation of the Spanwise Aerodynamic Loading." Princeton Univ. Aero. Engg. Deptt. Report No. 312. 1955.

9. R.B. Gray. "An Aerodynamic Analysis of a Single-Bladed Rotor in Hovering and Forward Flight as Determined from Smoke Studies of Vorticity Distribution in the Wake." Princeton Univ. Aero. Engg. Deptt. Report No. 356. 1955.

10. H. Lamb. "Hydrodynamics." 6th Edition, Dover, N.Y. 1945.

11. J.D. Kocurek and J.L. Tangler. "A Prescribed Wake Lifting Surface Hover Performance Analysis." Pre-Print 1001, 32nd Annual National Forum of AHS. May 76.

VITA

Satish S. Samant was born in Dombiwali, India in October 1949. He graduated from Sanjeewan Vidyalaya, Panchgani, in 1965. He attended the Elphinstone College, Bombay, for a period of one year and joined the Indian Institute of Technology, Bombay, where he earned his Bachelor of Technology degree in Aeronautical Engineering in 1971.

He joined the Georgia Institute of Technology, Atlanta in the fall of 1971 and earned his Master of Science in Aerospace Engineering degree in December 1972.

He is a student member of the American Helicopter Society and the American Institute of Aeronautics and Astronautics.

He is married to Jyoti.